Water retention curves of sandy soils in northern Poland

W. Gorczewska-Langner[1], A. Szymkiewicz[1], B. Jaworska-Szulc[1]

[1] Gdańsk University of Technology, Faculty of Civil and Environmental Engineering, Gdańsk Poland
Corresponding e-mail: wiogorcz@pg.edu.pl

GDAŃSK UNIVERSITY OF TECHNOLOGY

$$\theta(h) = \theta_r + \frac{\theta_s - \theta_r}{[1+|\alpha h|^n]^m}$$

Rien van Genuchten Conference

INTRODUCTION

Understanding soil hydraulic properties, particularly the soil water retention curve (SWRC), which describes the relationship between soil water potential and water content, is fundamental to a wide range of disciplines, including agriculture, hydrology, and civil and environmental engineering. The SWRC not only governs the movement and availability of water within the soil profile but also influences processes such as plant water uptake, irrigation management, and contaminant transport. In shallow, sandy aquifers typical of post-glacial regions of Northern Europe and North America, precise characterization of the SWRC is especially critical for evaluating groundwater recharge dynamics and assessing the susceptibility of these areas to pollution. Improving the accuracy of SWRC models is therefore essential for better predicting water balance components and for developing effective strategies for land and water resource management in vulnerable environments.

OBJECTIVES

- ✓ To evaluate various approaches for characterizing the hydraulic properties of sandy soil samples originating from young glacial deposits in northern Poland.
- ✓ To assess the feasibility of predicting SWRC based on fundamental soil physical properties, particularly particle size distribution.
- ✓ To analyze the performance of three variants of the Arya and Paris (1981) model (AP1, AP2, AP3) as well as the scaled versions of the Mohammadi and Vanclooster (MVS) and Chang and Cheng (2018) methods (CC), with particular attention to improving the representation of SWRC in the low water content range.
- ✓ To estimate soil water retention curves (SWRC) using three analytical models: the classical van Genuchten (1980) model (VG), the modified CS-VG model incorporating the Campbell and Shiozawa function for adsorbed water, and the BW-VG model integrating SWRC and hydraulic conductivity curves (HCC) across the full saturation range.
- ✓ To determine the parameters of the BW-VGM-PTF model based on standard van Genuchten-Mualem (VGM) model parameters and pedotransfer functions (PTFs) developed by Weber et al. (2020).

EXPERIMENTAL WORK

All methods were calibrated using drainage experiments conducted with a sand box and a sand/kaolin box apparatus supplied by Eijkelkamp Soil & Water. These devices enabled the determination of the soil water retention curve (SWRC) in the wet range, providing a foundation for further analyses and comparisons. SWRC was determined in the laboratory by measuring the drying branch of the curve. Saturated samples were placed on a sand layer covered with cloth and connected to a hanging water column, which allowed the application of stepwise increasing suction (h = 1, 2.5, 10, 32, 63, 100, 200, and 500 cm). The soil cores had a length of 5 cm, and the water potential was defined at the bottom of each sample. At each suction step, the samples were allowed to drain until equilibrium, and their water content was determined by weighing. In the sand/kaolin box setup, the sand fill was covered with a layer of kaolin, and suction was controlled using a vacuum vessel, enabling the application of higher suction values. The measurement process concluded with drying all tested samples in an oven, followed by their final weighing..

Fig. 1. Determination of the soil water retention curve (SWRC) using sand box and sand/kaolin box devices.

RESULTS

AP1, AP2, AP3, MVS AND CC MODELS

Table 1. Prediction errors of PTF functions.

Semi-physical PTFs	Total SSQ* [-]
AP1	0.219
AP2	0.239
AP3	0.215
CC	0.160
MVS	0.184
Average	0.203

** SSQ – sum of square errors between predicted and measured water content*

Table 2. Van Genuchten parameters fitted to SWRCs obtained using semi-physical PTFs.

Method	Parameter	L1	L2	L3	L4	L5	L6
All	q_s (-)	0.354	0.474	0.357	0.342	0.325	0.407
All except CC	q_r (-)	0	0	0	0	0	0
AP1	a (m^{-1})	1.690	2.120	2.400	5.700	5.490	4.430
	n (-)	2.500	3.925	3.741	2.420	1.975	1.796
AP2	a (m^{-1})	2.390	3.140	3.400	6.500	5.980	5.000
	n (-)	2.790	4.114	3.857	2.700	2.203	2.010
AP3	a (m^{-1})	2.090	2.460	2.970	9.300	9.440	7.320
	n (-)	2.242	3.826	3.606	2.185	1.786	1.625
MVS	a (m^{-1})	2.268	2.935	3.258	5.300	4.882	3.947
	n (-)	2.817	3.310	3.617	2.730	2.262	1.845
CC	q_r (-)	0	0	0.061	0.113	0.076	0.037
	a (m^{-1})	3.020	3.250	4.100	6.600	6.200	4.510
	n (-)	2.642	3.761	4.491	2.783	2.296	2.021

SOIL WATER RETENTION CURVE

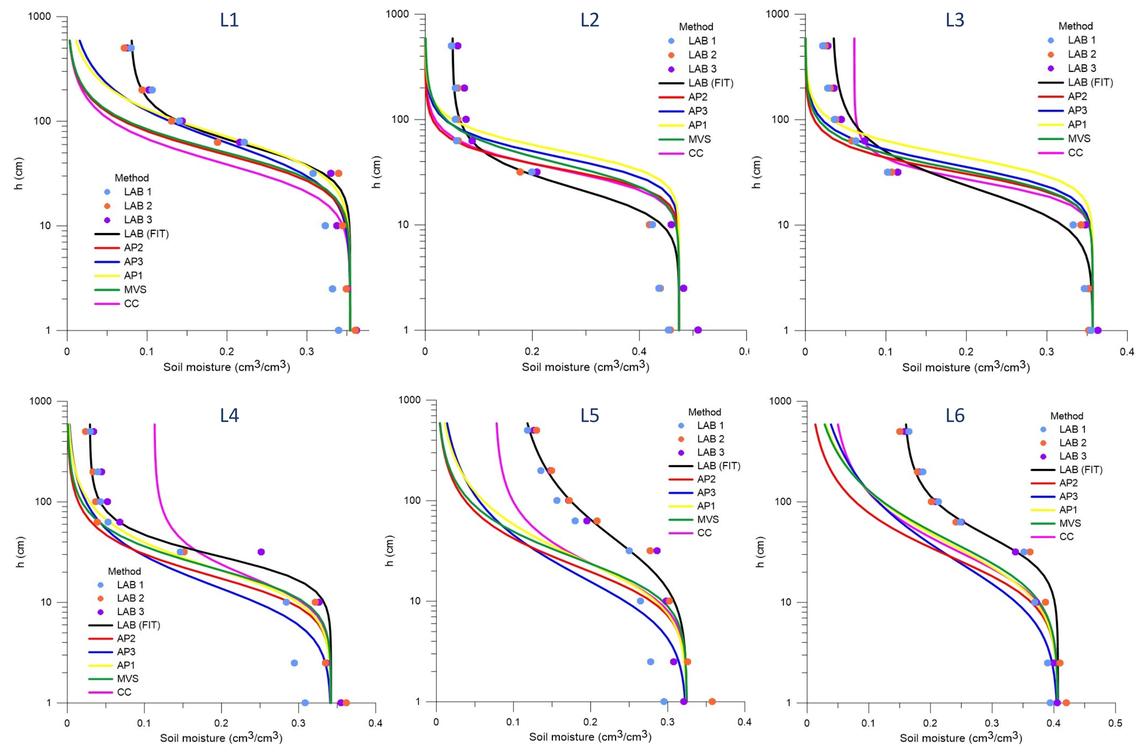

Fig. 2. SWRCs obtained from drainage experiments and selected PTFs for locations L1, L2, L3, L4, L5 and L6.

CS-VG, BW-VG, BW-VGM-PTF

Soil samples collected from location L7 at four sites (P1–P4) at various depths were used to estimate soil water retention curves (SWRC) with three analytical models — van Genuchten (VG), modified CS-VG, and BW-VG — and to determine BW-VGM-PTF parameters based on standard van Genuchten-Mualem (VGM) parameters and the pedotransfer functions (PTFs) developed by Weber et al. (2020). Samples were taken from depths of 3, 50, 65, and 100 cm at P1; 2, 20, 40, 45, and 80 cm at P2; 7, 20, 52, and 78 cm at P3; and 18, 30, and 40 cm at P4.

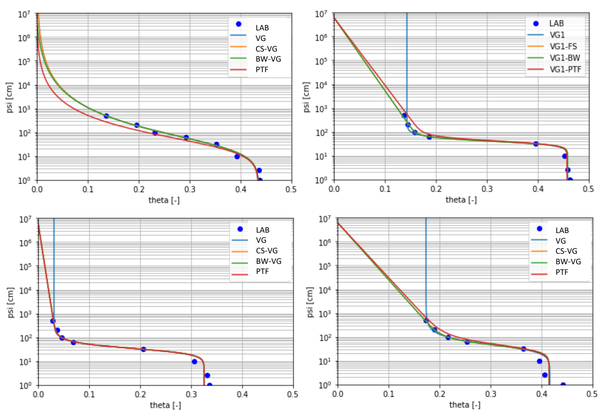

Fig. 3. SWRCs obtained from drainage experiments at location L7 at different depths.

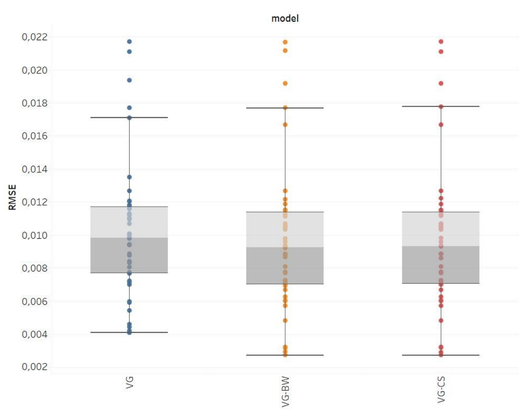

Fig. 4. RMSE values were estimated for all samples.

CONCLUSIONS

- ✓ The soils were classified into two groups based on the shape of their soil water retention curves (SWRC).
- ✓ The first group (L2, L3, L4) exhibited typical characteristics of clean sands with low fine fraction content, showing a sharp decrease in water content between 10 and 100 cm suction, followed by a linear decline at higher suctions.
- ✓ The second group (L1, L5, L6) showed higher water content at 100 cm suction and a steeper decline at greater suctions.
- ✓ Residual water content was generally higher in the second group, reflecting a greater proportion of adsorbed water, consistent with their higher content of fine particles (<0.125 mm).
- ✓ Gravel content had no significant impact on SWRC shape. These results highlight substantial variability in SWRC among sandy soils, primarily influenced by the finest particle fractions.
- ✓ Although more advanced models considering both capillary and adsorbed water could improve SWRC description in the dry range, this study focused on the standard van Genuchten model.
- ✓ The classic van Genuchten (VG) model does not accurately fit the SWRC in the dry range when only wet range data are available.
- ✓ The CS-VG, BW-VG, and BW-VGM-PTF models improve the fit in the dry range.
- ✓ Model comparison was based on RMSE values (Fig. 4).
- ✓ The average RMSE for CS-VG and BW-VG models is similar and lower than the VG model (CS-VG RMSE: 9.6211×10^{-3}; BW-VG RMSE: 9.6140×10^{-3}; VG RMSE: 10.2641×10^{-3}).

ACKNOWLEDGEMENTS

This work has been (partly) funded by National Center for Research and Development (NCBR, Poland) as part of EU Water4All project: WATER4ALL/I/37/AQUIGROW/2024 and the EU Horizon project SOILPROM (grant 101156589, soilprom.eu).

REFERENCES

- ✓ Arya, L. M., & Paris, J. F. (1981). A physicoempirical model to predict the soil moisture characteristic from particle-size distribution and bulk density data. *Soil Science Society of America Journal*, *45*(6), 1023-1030.
- ✓ Chang, C. C., & Cheng, D. H. (2018). Predicting the soil water retention curve from the particle size distribution based on a pore space geometry containing slit-shaped spaces, *Hydrology and Earth System Sciences*, *vol. 22*, no. 9, pp. 4621–4632.
- ✓ Van Genuchten, M. T. (1980). A closed-form equation for predicting the hydraulic conductivity of unsaturated soils. *Soil science society of America journal*, *44*(5), 892-898.
- ✓ Weber, T. K., Finkel, M., da Conceição Gonçalves, M., Vereecken, H., & Diamantopoulos, E. (2020). Pedotransfer function for the Brunswick soil hydraulic property model and comparison to the van Genuchten-Mualem model. *Water Resources Research*, *56*(9).

Soil Pore Space Structural Classification System (SPSCS): II- Application for Brazilian Latosols

Authors: Victor Matos dos Santos[1]*, Marta Vasconcelos Ottoni[1],

Theophilo Benedicto Ottoni Filho[2]

Rien van Genuchten Conference

Introduction

The porous structure of soils, determined by the shape, size, and arrangement of pores, influences the storage and dynamics of water and gases and the transport of solutes (OTTONI, 2024). Its characterization, although performed by different experimental methods (COLES et al., 1998; ROGASIK et al., 2003; LAL, 1991; HILLEL, 1998; CRAWFORD et al., 1995), lacks standardization, which led to the development of the Soil Pore Space Structural Classification System (SPSCS) by Ottoni (2017), a quantitative approach based on the volumetric structure of the pores and the similarity of air availability curves. This study applies the SPSCS to hydrophysical data from Brazilian Latosols, deep soils with high aggregate stability (KER, 1997; RESENDE et al., 2014), aiming to investigate the relationship between their structural classes and water and air capacities, aiming to contributing to a more precise and comprehensive understanding of the influence of the porous structure of Latosols on their hydraulic properties.

Objectives

To investigate the relationship between the structural classes of Brazilian Latosols, according to the SPSCS, and their hydric functionalities of aeration and hydration.

Material and Methods

- Data on water suction and volumetric water content from 45 Latosols samples were used, extracted from the HYBRAS database (Ottoni, 2018), covering physical, chemical, and soil structural data. Most samples have fine texture and blocky structure (Ottoni et al., 2024);
- The SPSCS system was applied, based on the air availability curve Aa(s) modeled by the van Genuchten (VG) equation, classifying soils into Orders, Sub-Orders, and Families;
- The Family gathers soils with similar air availability curves. These curves are a combination of the pore distribution curves, represented by the Orders, with the effective porosity represented by the Sub-Orders;
- The parameters θr, m, and α were adjusted with three suction points (60 cm, 330 cm, and 15000 cm) following a standardized protocol;

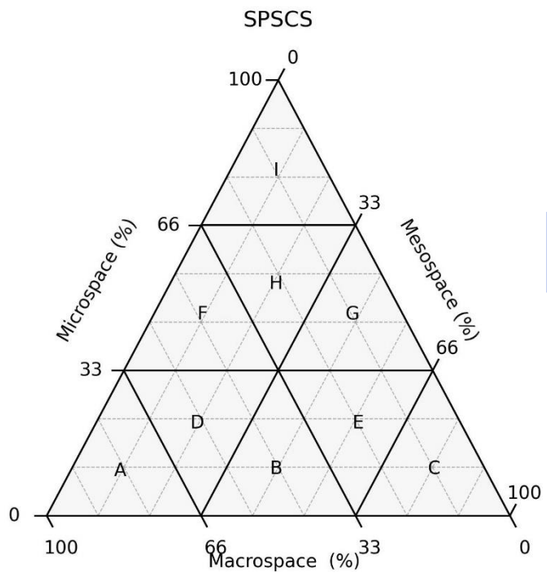

- Samples were categorized as genuine, adopted, or rejected based on ERRORMAX and RMSE30-18000 errors;
- Samples were grouped into air and water capacity classes.

Results

1. Classification

- Most of the samples (91.1%) were classified as genuine, 8.9% as adopted, and none as rejected;
- Genuine samples showed low adjustment errors (0.001 < RMSE < 0.033 cm³/cm³) and good adherence to the VG equation; adopted samples had errors between 0.035 and 0.043 cm³/cm³;
- Predominance of Order B (48.9%), followed by Orders A (22.2%) and D (14%). Family B2, with moderate macrospaces and mesospaces and moderate effective porosity, was the most frequent (33.3%). The Sub-Order 2 was the most common (56.6%) followed by 3 (31,1%) and 1 (13,3%).

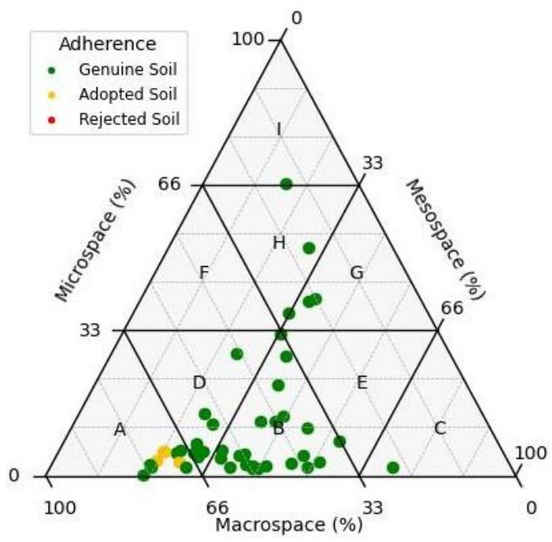

2. Relations with Hydraulic Functionalities

- Sub-Order 1, with six samples from Order B, macro-mesospaced, presented restrictions in water and air capacities;
- Sub-Order 2, with 25 soils distributed among Orders B, D, A, G, H, and C, with most samples presenting water capacity restrictions;
- Sub-Order 3, with ten samples, had a predominance of soils without air and water capacity restrictions.

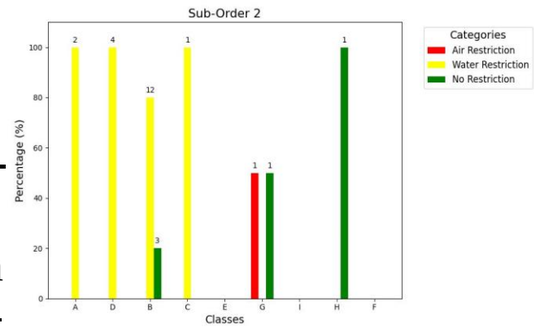

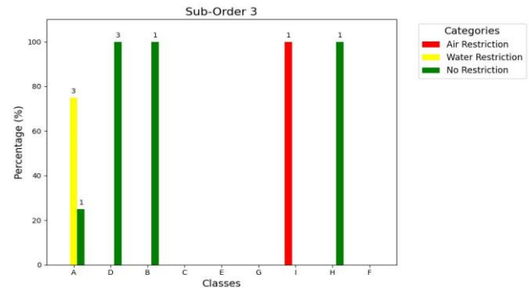

Conclusions

- Most Latosol samples are genuine soils, with good adherence and low errors in the van Genuchten water retention model;
- Macrospacious classes A and D, hybrid class B, and Sub-Order 2 with moderate effective porosity predominated;
- Most Latosols showed no air capacity restriction but 58% showed restricted available water for root use;
- The methodology and SPSCS proved effective for functional characterization and structural classification of porous spaces.

[1] Geological Survey of Brazil, Department of Hydrology, Rio de Janeiro/RJ, Brazil

* Speaker

[2] Universidade Federal do Rio de Janeiro (UFRJ), Department of Water Resources and Environment, Rio de Janeiro, RJ, Brazil

CPRM Serviço Geológico do Brasil

UFRJ

ANALYZING MACRO AND MICROPOROSITY WITH μCT IMAGES FOR IMPROVING NMR AND RESISTIVITY INTERPRETATION

Silvia B. Bermudez[1,2], Gabriel S. Ribeiro[1,2], Austin Boyd[2], Maira O. Lima[2], Tiago Pineiro[2], Andres Zuniga[2,3], Paulo Couto[2]

[1]*Civil Engineering Program, COPPE, Federal University of Rio de Janeiro, Brazil*

[2]*Enhanced Oil Recovery Laboratory, LRAP+/COPPE/, Department of Civil Engineering, Federal University of Rio de Janeiro, Brazil*

[3]*Trident Energy, Brazil Ltda.*

INTRODUCTION

The 3D μCT images made it possible to identify macropores (radii > 4 μm), but did not detect microporosity, which is common in carbonates, due to the resolution limit. Although microporosity depends on connectivity, it significantly influences electrical properties and NMR responses, making it difficult to distinguish between macro- and micropores in the T_2 distribution, especially due to diffusive coupling. In electrical data, this microporosity can generate low cementation index (*m*) values, affecting oil saturation calculations. To get around image limitations, the Density Equation ("Law of Mixtures") was applied, using pixel values as apparent density proxies, improving the identification of micropores. This study analyzed carbonate rock samples from the Morro do Chaves Formation (SE-AL Basin), using μCT, NMR, resistivity and gas porosimetry (RCAL).

GEOLOGICAL SETTING

This study analyzed five carbonate core samples from the Morro do Chaves Formation in the SE-AL Basin, a pre-salt reservoir analogue. The coquinas, from Barremian–Aptian outcrops in the Pedreira Atol region (São Miguel dos Campos, Alagoas), are interbedded with laminates, sandstones, and conglomerates.

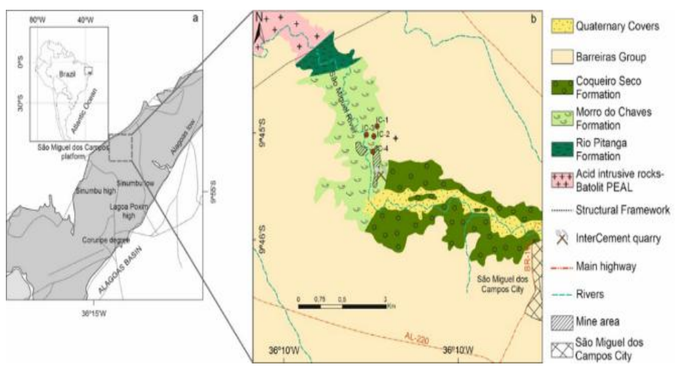

Figure 1 – a) Location of the Alagoas Sub-Basin in northeastern Brazil showing the São Miguel dos Campos platform in detail. b) Geological map of Upper Cretaceous of Alagoas Sub-Basin (Modified from Garcia et al.,2018)

METHODOLOGY

The samples underwent μCT imaging, NMR and Resistivity analysis and laboratory gas porosimetry (RCAL). The Density Equation, also known as the 'Law of Mixtures', was applied to enhance microporosity identification in CT images, using μCT pixel values as proxies for apparent density. Since the 1-inch diameter core samples were subjected to RCAL analysis, to obtain experimental porosity values before subsequently acquired images on the μCT, the Density Equation can be expressed as follows (Eq. 1)

$$\emptyset_{\mu CT} = \frac{CT_{Matrix} - CT_{Average}}{CT_{Matrix} - CT_{Fluid}} \quad (1)$$

Here, $\emptyset_{\mu CT}$ represents the porosity obtained from RCAL, while $CT_{Average}$ is the mean voxel value core image. If CT_{Matrix} is known, CT_{Fluid} can be determined, and vice-versa. Once one or both values are established through histogram analysis of μCT values, voxel-specific porosity can be calculated using (Eq. 2)

$$\emptyset_{pixel} = \frac{CT_{Matrix} - CT_{pixel}}{CT_{Matrix} - CT_{Fluid}} \quad (2)$$

The resistivity of each pixel was calculated by the Archie equation, using the porosity $\emptyset_{pixel}$ (Eq. 2), the specific *m* value of each sample (Table 1) and assuming R_w=0.07 Ω·m at 75 °F (Eq. 3).

$$R_{pixel} = \frac{R_W}{\emptyset_{pixel}^m} \quad (3)$$

FRAMEWORK

Step 1	Preparing samples and basic petrophysics	μCT image acquisition NMR acquisition Resistivity acquisition
Step 2	Histogram analysis to define CT_{Matrix} and CT_{Fluid}	$\emptyset_{\mu CT} = \frac{CT_{Matrix} - CT_{Average}}{CT_{Matrix} - CT_{Fluid}}$
Step 3	Application of the Density Equation	$\emptyset_{pixel} = \frac{CT_{Matrix} - CT_{pixel}}{CT_{Matrix} - CT_{Fluid}}$
Step 4	Generating the Porosity Map	Figure (2)
Step 5	Generating the Resistivity Map based on the $\emptyset_{pixel}$	$R_{Pixel} = \frac{R_w}{\emptyset_{pixel}^m}$
Step 6	Comparison with the Porosity Map generated in ImageJ	Figure (2)

RESULTS AND DISCUSSION

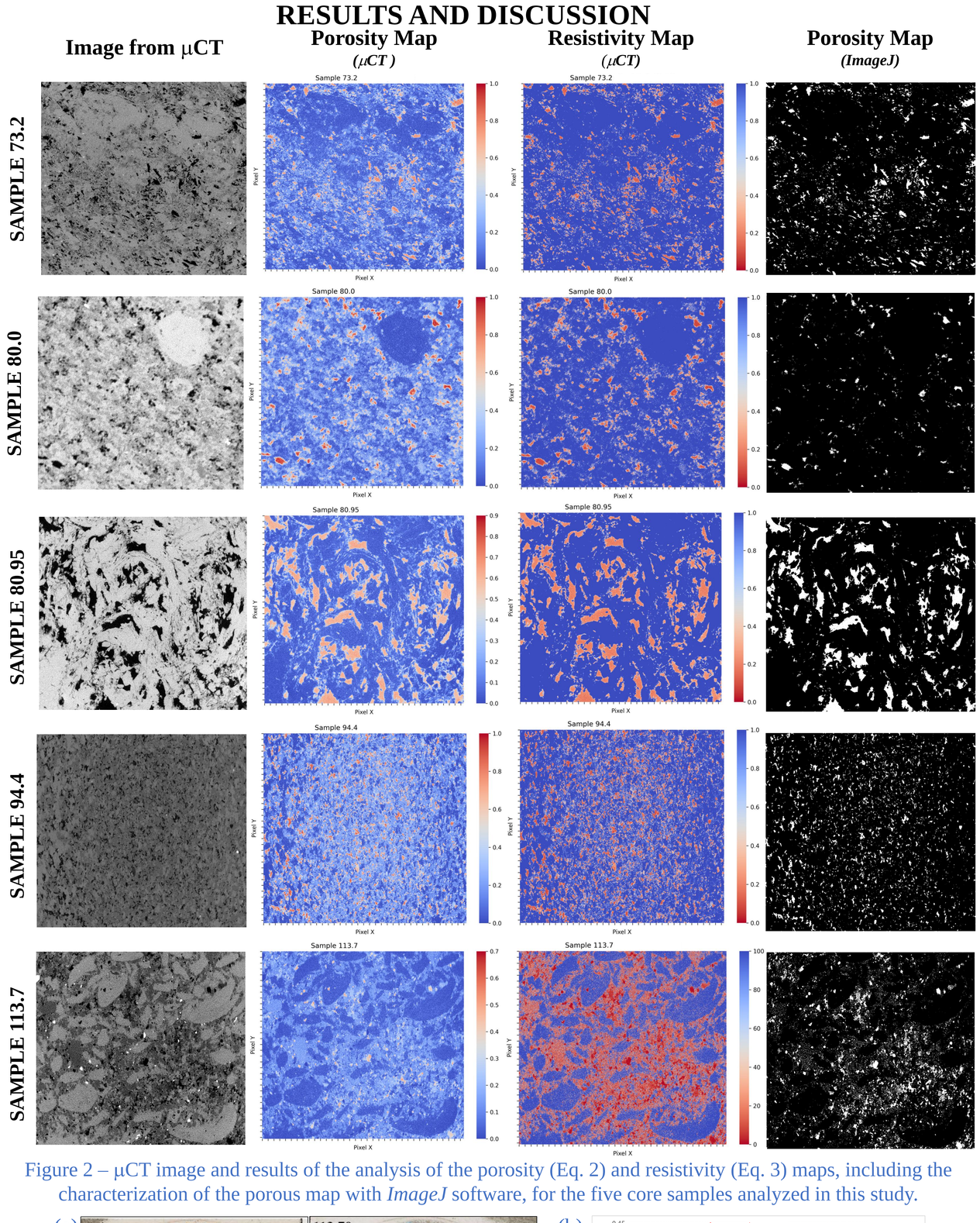

Figure 2 – μCT image and results of the analysis of the porosity (Eq. 2) and resistivity (Eq. 3) maps, including the characterization of the porous map with *ImageJ* software, for the five core samples analyzed in this study.

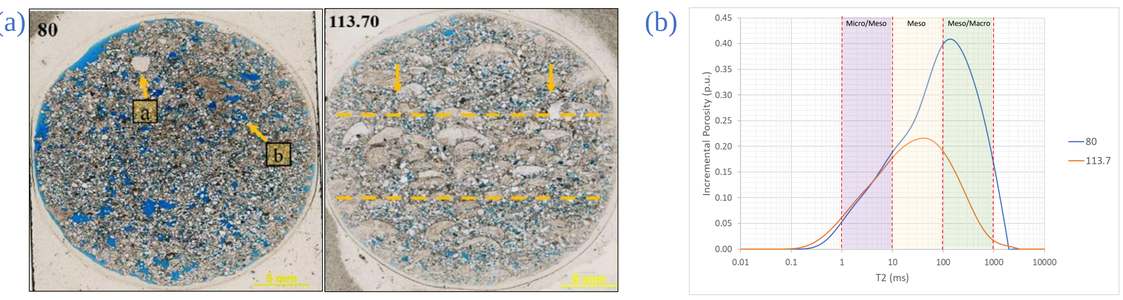

Figure 3 – (a) Thin section from samples 80 and 113.70. (b) T_2 distribution and the pore size partitioning.

Table 1 – Routine porosity (ϕ_{He}), porosity estimated from NMR (ϕ_{NMR}), porosity estimated by Eq. (1) from μCT ($\phi_{\mu CT}$), porosity obtained with ImageJ (ϕ_{ImageJ}), routine permeability (*k*) and cementation exponent values (*m*) for each sample.

Samples	ϕ_{He} (%)	ϕ_{NMR} (%)	$\phi_{\mu CT}$ (%)	ϕ_{ImageJ} (%)	*k*(mD)	*m*
73.2	18.8	17.7	18.6	6.13	71	2.154
80.0	16.0	15.4	21.8	2.12	24	2.390
80.95	19.6	17.5	17.4	13.05	504	2.131
94.4	18.5	17.9	22.7	6.68	103.5	1.953
113.7	8.7	8.9	9.9	10.02	0.433	2.856

CONCLUSION

- ✓ The pixel-by-pixel approach based on the density equation proves effective for estimating porosity and resistivity, even in the presence of unresolved microporosity;
- ✓ The methodology is consistent with experimental RCAL and NMR data and complements traditional segmentation tools;
- ✓ The technique has potential application in complex rock environments, such as pre-salt carbonates, where NMR and resistivity interpretation depend heavily on pore connectivity.

FUTURE WORK

- ✓ We plan to evaluate the porosity and resistivity matrices using voxel in 3D.
- ✓ Make a closer analysis between the resistivity values and the different mineralogies of the rock.
- ✓ Use of Weka artificial intelligence integrated with ImageJ to optimize microporosity analysis

REFERENCES

Ramakrishnan, T.S. et al., *A Model-Based Interpretation Methodology for Evaluating Carbonate Reservoir*. SPE Annual Technical Conference and Exhibition, Sep 30 – Oct 03, 2001.

Garcia, G.G., et al., *Palynology of the Morro do Chaves Formation (lower Cretaceous), Sergipe Alagoas Basin, NE Brazil: Paleoenvironmental implications for the early history of the South Atlantic*. Cretaceous Research, vol. 90, pp. 7–20, 2018.

This research was carried out in association with the ongoing R&D project registered as ANP nº 23020-1, "Análise Experimental da Recuperação Avançada de Petróleo em Reservatórios Carbonáticos do Pré-Sal do Brasil Através de Injeção Alternada de CO2 e Água – Fase II - Condições de Reservatório" (UFRJ/Shell Brasil/ANP), sponsored by Shell Brasil Petróleo Ltda under the ANP R&D levy as "Compromisso de Investimentos com Pesquisa e Desenvolvimento".

Plant available water
proposal of a flux-based approach

Quirijn de Jong van Lier
CENA – University of São Paulo, Brazil

Introduction

Plant available water (PAW) is widely used in agriculture to assess soil suitability for crop growth and irrigation planning, and in ecology to understand plant distribution and ecosystem hydrology. In reservoir models, PAW supports simulations of the soil water balance. Traditionally, total available water (TAW) is defined as the difference between field capacity (FC) and wilting point (WP), while readily available water (RAW) spans from FC to a limiting point (LP). These thresholds are usually estimated using static pressure head values, though they can vary with soil and plant characteristics. Flux-based approaches offer a more dynamic alternative, using soil hydraulic properties and process-based root water uptake models. These models integrate soil, plant, and atmospheric parameters to estimate transpiration and water uptake. Hydrological models such as Hydrus and SWAP have incorporated such approaches, though their use remains limited, especially applied to tropical regions due to a lack of quality soil data. To address this, in this study the flux-based method MFLUX is applied to 20 tropical soil profiles in southeast Brazil, comparing results with traditional (static) estimates and evaluating the propagation of parameter uncertainty in soil hydraulic modeling.

Objectives

- Interpret the results of a detailed hydraulic characterization of 20 tropical soils from southeast Brazil to predict plant available water by a flux-based approach
- Discuss the outcomes in the light of long-term simulations of soil water balance components under the local climate and an annual crop (maize).

Material and Methods

Soil hydraulic properties

Soil hydraulic properties for two layers of twenty southeast Brazilian soils (Ferralsols, Acrisols, and Nitisols, all sampled around coordinates 23° S and 47.5° W, Figure 1) were obtained from a series of determinations using a tension table (-10 - -600 cm), HyProp equipment (-50 - -1000 cm), pressure chamber (-1000 and -3000 cm), WP4 dewpoint meter (-10,000 - -30,000 cm) and a KSAT falling head permeameter. All data together were used in a fitting procedure to yield VGM parameters (Table 1), standard errors, and correlation coefficients

Soil ID	WRB Soil Order	Depth	Bulk density	Clay	Content Silt	Sand	α	n	K_{sat}	l	θ_s	θ_r
		cm	kg m^{-3}		kg kg^{-1}		cm^{-1}		cm d^{-1}		m^3 m^{-3}	
P1	Arenosol	5-10	1699	0.152	0.036	0.811	0.038	1.362	54	1.55	0.338	0.077
		20-25	1770	0.177	0.017	0.806	0.033	1.445	77	2.08	0.341	0.094
P2	Cambisol	5-10	1676	0.206	0.194	0.601	0.147	1.054	9707	8.20	0.360	-0.315
		20-25	1615	0.178	0.168	0.654	0.024	1.525	114	1.32	0.384	0.087
P3	Ferralsol	5-10	1530	0.653	0.087	0.260	0.044	1.203	18	-0.63	0.459	0.271
		20-25	1439	0.703	0.055	0.242	0.021	1.224	41	2.68	0.437	0.221
P4	Nitisol	5-10	1443	0.517	0.209	0.273	0.102	1.197	1068	1.20	0.455	0.250
		20-25	1435	0.515	0.183	0.302	0.097	1.257	382	0.72	0.455	0.246
P5	Lixisol	5-10	1144	0.595	0.114	0.291	0.267	1.183	1095	-1.18	0.585	0.057
		20-25	1361	0.698	0.068	0.233	0.096	1.600	260	-0.60	0.477	0.292
P6	Ferralsol	5-10	1050	0.449	0.214	0.337	0.199	1.395	1205	-0.89	0.596	0.167
		20-25	1349	0.470	0.206	0.324	0.343	1.282	891	-1.91	0.489	0.157
P7	Ferralsol	5-10	1146	0.317	0.127	0.556	0.614	1.287	1082	-2.63	0.555	0.121
		20-25	1346	0.313	0.137	0.550	0.303	1.272	1475	-1.95	0.492	0.079
P8	Acrisol	5-10	1191	0.410	0.118	0.473	0.055	1.136	232	2.93	0.529	0.052
		20-25	1377	0.610	0.063	0.327	0.386	1.165	593	-2.39	0.480	0.295
P9	Gleysol	5-10	1168	0.332	0.088	0.580	0.477	1.188	940	-3.39	0.545	0.090
		20-25	1274	0.375	0.093	0.532	0.113	1.358	346	-1.46	0.493	0.202
P10	Cambisol	5-10	1197	0.308	0.052	0.640	0.199	1.621	1122	-0.50	0.540	0.138
		20-25	1280	0.355	0.058	0.587	0.131	1.603	1420	-1.05	0.505	0.159
P11	Ferralsol	5-10	1336	0.306	0.080	0.614	0.320	1.257	1955	-2.49	0.501	0.054
		20-25	1419	0.359	0.107	0.534	0.131	1.364	228	-2.39	0.462	0.118
P12	Ferralsol	5-10	1136	0.523	0.039	0.439	0.283	1.571	1427	-1.26	0.567	0.202
		20-25	1219	0.363	0.040	0.597	0.116	1.578	970	-0.73	0.539	0.233
P13	Acrisol	5-10	1486	0.253	0.042	0.706	0.086	1.602	306	-1.28	0.424	0.136
		20-25	1335	0.495	0.030	0.475	0.160	1.374	267	-2.51	0.488	0.209
P14	Ferralsol	5-10	1209	0.523	0.174	0.303	0.346	1.301	1935	-0.40	0.543	0.196
		20-25	1466	0.538	0.184	0.277	0.093	1.223	681	4.52	0.438	0.228
P15	Gleysol	5-10	1299	0.217	0.130	0.653	0.011	1.182	26	2.57	0.468	-0.090
		20-25	1600	0.256	0.132	0.612	0.031	1.181	152	2.93	0.386	0.061
P16	Ferralsol	5-10	1605	0.656	0.098	0.247	0.050	1.033	2332	17.40	0.395	-0.199
		20-25	1368	0.708	0.077	0.215	0.076	1.130	183	0.36	0.452	0.131
P17	Ferralsol	5-10	1506	0.215	0.188	0.596	0.374	1.172	512	-4.06	0.418	0.032
		20-25	1541	0.254	0.184	0.562	0.166	1.221	207	-3.32	0.412	0.040
P18	Ferralsol	5-10	1204	0.439	0.288	0.273	0.112	1.243	81	-1.27	0.535	0.261
		20-25	1507	0.517	0.248	0.234	0.062	1.227	88	-0.54	0.424	0.173
P19	Ferralsol	5-10	1481	0.576	0.112	0.311	0.226	1.134	100	-7.16	0.435	0.108
		20-25	1512	0.577	0.122	0.301	0.083	1.239	35	-3.36	0.413	0.202
P20	Acrisol	5-10	1097	0.349	0.157	0.494	0.551	1.290	433	-1.34	0.584	0.319
		20-25	1504	0.428	0.131	0.441	0.108	1.135	313	6.66	0.424	0.094

Table 1 – Basic information about the sampled soils and VGM parameters.

Figure 1 – Map of Brazil and surrounding countries indicating the region of soil sampling.

Generating stochastic parameter realizations

To improve the normality of the hydraulic parameters, parameter transforms were applied according to Carsel & Parrish (1988), i.e.,

$$\kappa = \ln(K_s) \Leftrightarrow K_s = e^{\kappa}$$
$$\tau = \ln(\alpha) \Leftrightarrow \alpha = e^{\tau}$$
$$\nu = \ln(n-1) \Leftrightarrow n = 1 + e^{\nu}$$

The means and standard deviations of the transformed parameters and their correlation matrix were used to generate 10^4 stochastic parameter realizations for each layer of the soils using a Cholesky decomposition performed by the software StochHyProp (De Jong van Lier, 2023). The resulting transformed parameter realizations were untransformed to their original VGM values for use in a hydrological model.

Threshold values for Plant Available Water

Field capacity (FC) was determined simulating an internal drainage experiment using the SWAP hydrological model (Kroes et al., 2017), starting at saturation. FC was considered to correspond to the hydraulic conditions when the bottom flow at a depth of 60 cm was less than 1 mm d^{-1}.

The **limiting point (LP)**, defining the onset of the falling rate phase of crop transpiration was calculated using the equation by Pinheiro et al. (2017) yielding the corresponding matric flux potential M_{LP} (cm^2 d^{-1}) given by

$$M_{LP} = \int_{h_{ref}}^{h_{LP}} K dh = \frac{5.3 T_p}{\pi \sum_{i=1}^{k} L_i R_i}$$

where K is the hydraulic conductivity, h_{ref} = -1.5·10^4 cm, h_{LP} (cm) is the pressure head at the limiting point, T_p (cm d^{-1}) is the potential transpiration taken as 0.4 cm d^{-1}, k is the number of layers (k = 2), L_i (cm) is the thickness of layer i (here: 20 and 40 cm, respectively), and R_i (cm cm^{-3}) is the root length density per layer. R_1 = 1 cm cm^{-3} and R_2 = 0.1 cm cm^{-3} was applied.

The **wilting point (WP)** was predicted applying a factor f_{WP} = 0.01 to M_{LP}: $M_{WP} = \int_{h_{ref}}^{h_{WP}} K dh = f_{WP} M_{LP}$

These threshold values for plant available water expressed as soil water content (θ) were used to calculate the **total available water** (TAW = $\theta_{FC} - \theta_{WP}$) and the **readily available water** (RAW = $\theta_{FC} - \theta_{LP}$) contents. For comparison to the traditionally determined value of TAW based on static values of pressure head for FC and WP, a "static TAW" (sTAW) was calculated as sTAW = $\theta_{pF2} - \theta_{pF4.2}$.

Crop simulation scenarios

Simulations were performed with the hydrological model SWAP, v. 4.2.32 (Kroes et al., 2017), a 1-D model that numerically solves a discretized version of the Richards equation with a sink term (root water uptake) describing vertical water flow in the soil-plant-atmosphere environment. SWAP makes use of the Van Genuchten-Mualem soil hydraulic parameterization. The simulation of transpiration and growth reduction due to water stress was performed using the process-based RWU function MFlux (De Jong Van Lier et al., 2013).

A rainfed maize crop was simulated with a maximum rooting depth of 60 cm and root length density linearly decreasing with depth. Weather data were retrieved from the meteorological station of the University of São Paulo in Piracicaba, Brazil (22.7° S; 47.6° W, 526 m asl, Koeppen Cwa). The crop cycle was defined at 111 days and started on 01/Dec of each simulated year (ending 21/March of the subsequent year). The simulations covered three rainfall scenarios: an average year (2012-2013) with 1330 mm of total rainfall (674 mm during the growing season), a dry year (2013-2014) with 816 mm of total rainfall (371 mm during the growing season), and a wet year (1998-1999) with 1628 mm of total rainfall (1033 mm during the growing season). Reference ET was calculated by the Penman-Monteith equation applying the FAO methodology (Allen et al., 1998) to predict the potential evapotranspiration from a vegetated surface using crop resistance, crop height, and reflection coefficient.

Results / Discussion

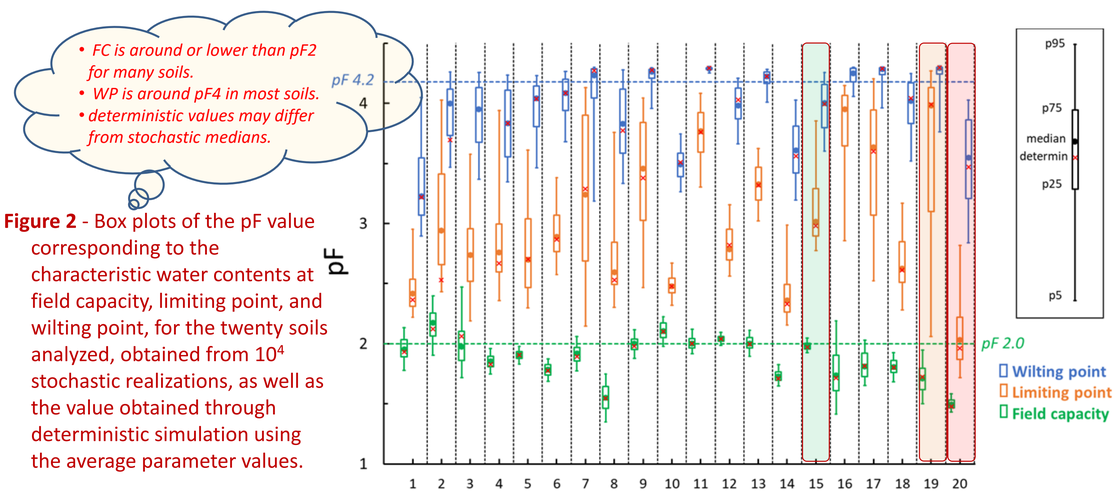

Figure 2 - Box plots of the pF value corresponding to the characteristic water contents at field capacity, limiting point, and wilting point, for the twenty soils analyzed, obtained from 10^4 stochastic realizations, as well as the value obtained through deterministic simulation using the average parameter values.

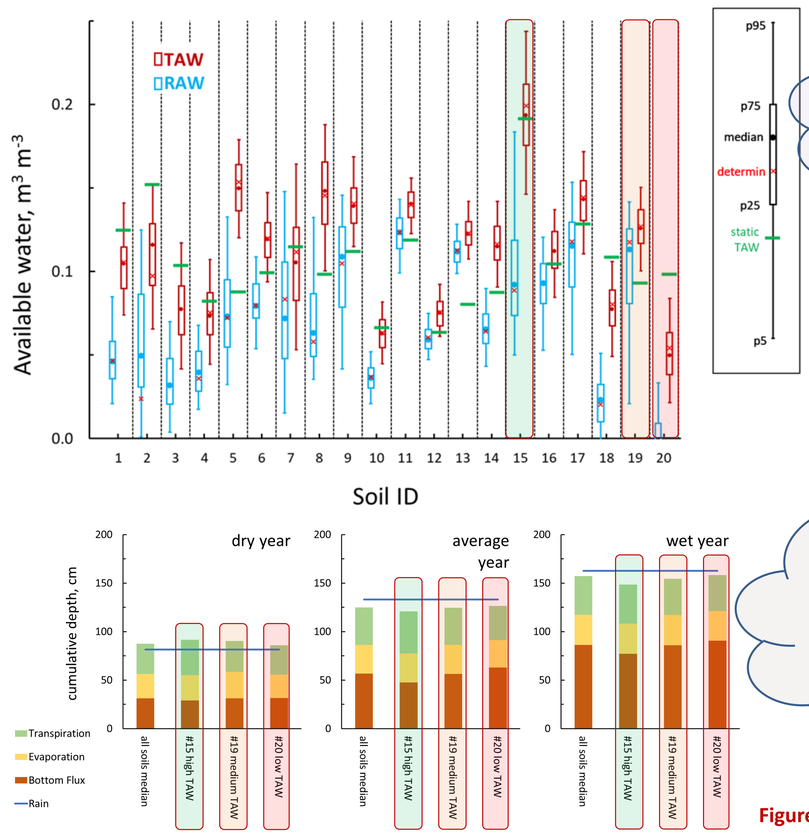

• *sTAW correlates to TAW, but may be higher or lower than TAW (e.g. soils 19 and 20).*
• *Deterministic values for TAW and RAW differ from stochastic medians in some soils.*

Figure 3 - Box plots of TAW and RAW for the twenty soils obtained from 10^4 stochastic realizations, as well as the value obtained through deterministic simulation, and the static TAW (sTAW) calculated based on pF_{FC} = 2 and pF_{WP} = 4.2.

• *T+E+BF > R in a dry year and <R in an average or wet year*
• *low TAW soils drain more and transpire less than high TAW soils*
• *total water use of a low TAW soil is higher than for a high TAW soil in average or wet years.*
• *TAW reflects soil water balance components better than sTAW (cf. soils 19 and 20)*

Figure 4 - Observed cumulative rainfall and water balance components predicted for the twenty soils, and for a high, medium and low-TAW soil, in a dry, average, and wet year (medians from 10^4 stochastic realizations).

Conclusions

1. TAW and RAW calculated using static pressure head definitions may differ from flux-based predictions, and flux-based predictions of TAW and RAW seem to correlate better to soil water balance components.
2. Flux-based field capacity medians corresponded to pF-values between 1.5 and 2.3, limiting points ranged from 2.0 to 3.9, and wilting points varied between 3.2 and 4.3.
3. A greater versatility of the flux-based method and its stronger alignment with soil water balance components was shown in comparison to the traditional (static) method;
4. Disadvantages of the flux-based method include the greater need for detailed soil information (full soil hydraulic properties) and an increased computational effort;
5. No correlation of TAW and RAW, and clay content is found in these tropical soils;
6. Uncertainty in estimating soil hydraulic properties and related outputs (e.g., TAW, RAW, water balance) can be assessed via stochastic modeling. It affects practices like irrigation and land evaluation and can be minimized through improved sampling, lab methods, and selection of appropriate hydraulic models.
7. Median values of stochastic simulations for characteristic water contents and soil water balance components may differ significantly from the results of deterministic simulations, and stochastic predictions including parameter uncertainties may be preferred;

Acknowledgements

This research was supported by the São Paulo Research Foundation (FAPESP), project 2022/00853-2

Cited literature

Allen, R.G., Pereira, L.S., Raes, D., Smith, M., 1998. Crop evapotranspiration. Guidelines for computing crop water requirements. FAO Rome.
Carsel, R.F., and R.S. Parrish. 1988. Developing joint probability distributions of soil water retention characteristics. Water Resour. Res. 24(5): 755–769.
De Jong van Lier, Q. 2023. StochHyProp: A software to generate stochastic realizations of correlated parameters dedicated to soil hydraulic properties. Softw. Impacts 15: 100483.
De Jong Van Lier, Q., J.C. Van Dam, A. Durigon, M.A. Dos Santos, and K. Metselaar. 2013. Modeling water potentials and flows in the soil–plant system comparing hydraulic resistances and transpiration reduction functions. Vadose Zone J. 12(3).
Kroes, J.G., J.C. Van Dam, R.P. Bartholomeus, P. Groenendijk, M. Heinen, et al. 2017. SWAP version 4; Theory description and user manual. https://edepot.wur.nl/416321.

Evaluating the Permeability of Carbonate Rocks by using Critical Path Analysis and combining MICP and NMR Measurements

Elizabeth M. Pontedeiro[1,2*], **Paulo H. S. Moreira[1]**, Maira C. O. Lima[1], Gabriel S. S. Ribeiro[1], Silvia L. B. Bermudez[1], Paulo Couto[1]

[1]*LRAP+, Program of Civil Engineering, Federal University of Rio de Janeiro, Brazil*

[2]*Department of Earth Sciences, Utrecht University, The Netherlands*

1. Introduction

The primary objective was to utilize NMR and MICP data from a collection of coquina plugs associated with a well to optimize the van Genuchten hydraulic parameters. Using a *Critical Path Analysis,* it was possible to determine the critical radius and verify correlations with the measured permeability. Additionally, results obtained using well tools were employed to categorize the plugs into specific rock types and obtain correlations between the critical radius and the measured permeability.

2. NMR and MICP

Mercury intrusion capillary pressure (MICP) and nuclear magnetic resonance (NMR) are widely used to probe the pore systems of porous media, with applications determining the permeability. MICP may be used to compute percolation threshold of a sample (Daigle & Johnson, 2016). NMR relaxation time distributions on the other hand may be used to determine the pore size distribution, It is common to compare NMR relaxation time distributions to MICP pore throat size distributions to obtain an NMR proxy for pore size. The standard technique for combining NMR and MICP data to allow direct calculation of pore sizes from NMR data is cross-correlation of the incremental pore throat size distribution from MICP with the NMR T_2 distribution.

For this study we used 44 plugs of carbonate rocks (coquinas) taken from the Morro do Chaves Formation in Northeastern Brazil. Morro do Chaves was formed by the accumulation of coquinas (shells of bivalve mollusc and shales from lacustrine environments), interspersed with siliciclastic rocks. The samples belonged to a single well, with the rock being very heterogeneous, specially regarding porosity and permeability. We performed basic petrophysics and NMR measurements for the entire sample set, and MICP measurement of 21 samples.

Example of coquina samples

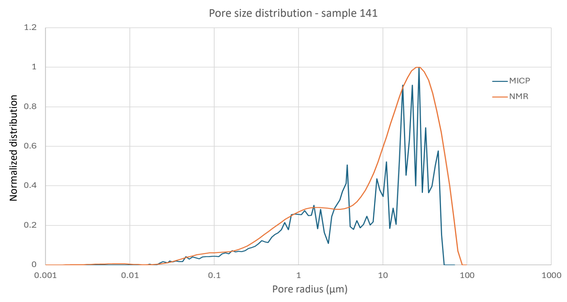

Matched NMR and MICP curves

Our primary objective was to utilize NMR and MICP data from the plugs to optimize the estimate the van Genuchten (VG) hydraulic parameters. Additionally, results obtained using well tools were employed to group the plugs into specific rock types. Fluid retention curves were obtained from the results of the NMR T_2 (with T_2 transformed into pore radius) and the mercury intrusion experiments, to obtain estimates of the unsaturated van Genuchten unsaturated hydraulic parameters.

3. Critical Path Analysis

Percolation theory provides a theoretical framework from statistical physics to address the effect of interconnectivity on fluid flow in heterogeneous media such as soils and rocks. Critical path analysis (CPA) is a promising technique from percolation theory. According to the CPA, flow through porous media is controlled by pore throats whose sizes are greater than some critical value (the critical pore-throat radius). Within the CPA framework, pore throats with radii greater than the critical pore-throat radius should significantly contribute to fluid flow (Ghanbarian & Skaggs, 2022).

In this work we used the Critical Path Analysis to determine the critical pore radius (r_c) given by:

$$r_c = 0{,}149/\ h_{inf} \qquad (1)$$

where,

$$h_{inf} = (1/\alpha)\ (1/m)^{1/n} \qquad (2)$$

In which **α**, **m** and **n** are the VG parameters. The critical radius can also be obtained from the inflection point of the cumulative mercury saturation curve where the second derivative is zero, while the first derivative (the slope of the curve) is zero where the peak of the incremental PSD curve occurs. We evaluated the correlation of the percolation radius (instead of total porosity) and the measured permeability, as well as correlations of the measured permeability with estimated permeabilities from the critical radius and the Katz-Thompson equation.

Table 1 – Correlation Measured Perm x Rcrit

Well (44 Coquinas)	R^2
Perm x $r_{critNMR}$	0.85
Perm x $r_{critMICP}$	0.79
Perm x r_{critIP}	0.84

Table 2 – Correlation Measured x Evaluated Perm

Well (44 Coquinas)	R^2
Perm x Estimated Perm ($r_{critNMR}$)	0.60
Perm x Estimated Perm ($r_{critMICP}$)	0.64
Perm x Estimated Perm (r_{critIP})	0.72

4. Rock type

Our aim to group carbonate rocks with similar petrophysical responses is to reduce reservoir heterogeneity in further analyses. Based on this concept, this study refines the framework proposed by Lima-Santo (2020) for the coquinas by incorporating additional characterization techniques. The current methodology integrates well log data (resistivity, compressional sonic transit time), routine core analysis (porosity, /permeability), thin section petrography, and X-ray diffraction (XRD) and NMR measurements. The integration enabled the definition of three distinct rock types (i.e., Reservoir, Closed and Hybrid Coquinas) with the objective of representing the heterogeneity of the pore system and its influence on fluid flow.

The Reservoir group exhibited the highest permeabilities (199.12 mD), with a predominance of connected vuggy and moldic pores that enhanced fluid flow efficiency. The Closed Coquinas group is characterized by low porosity and permeability, associated with high resistivity values and reduced compressional sonic transit times. The Hybrid Coquina group, in turn, combined siliciclastic and carbonate fragments, resulting in the highest average porosity among the groups (18.05%) and an intermediate permeability (86.45 mD).

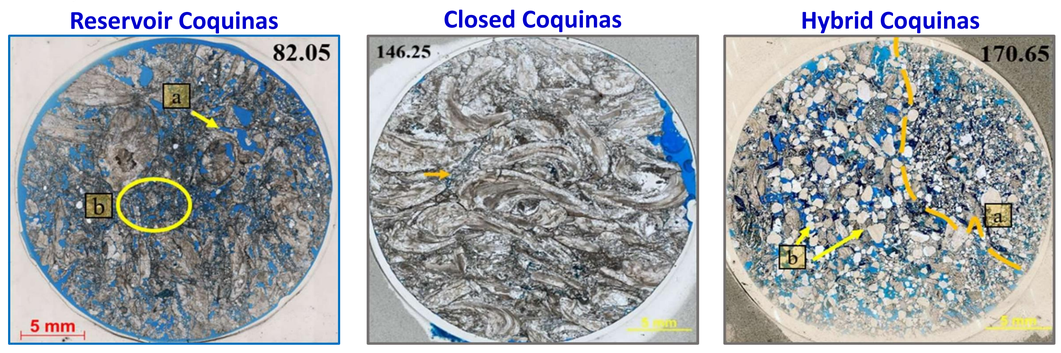

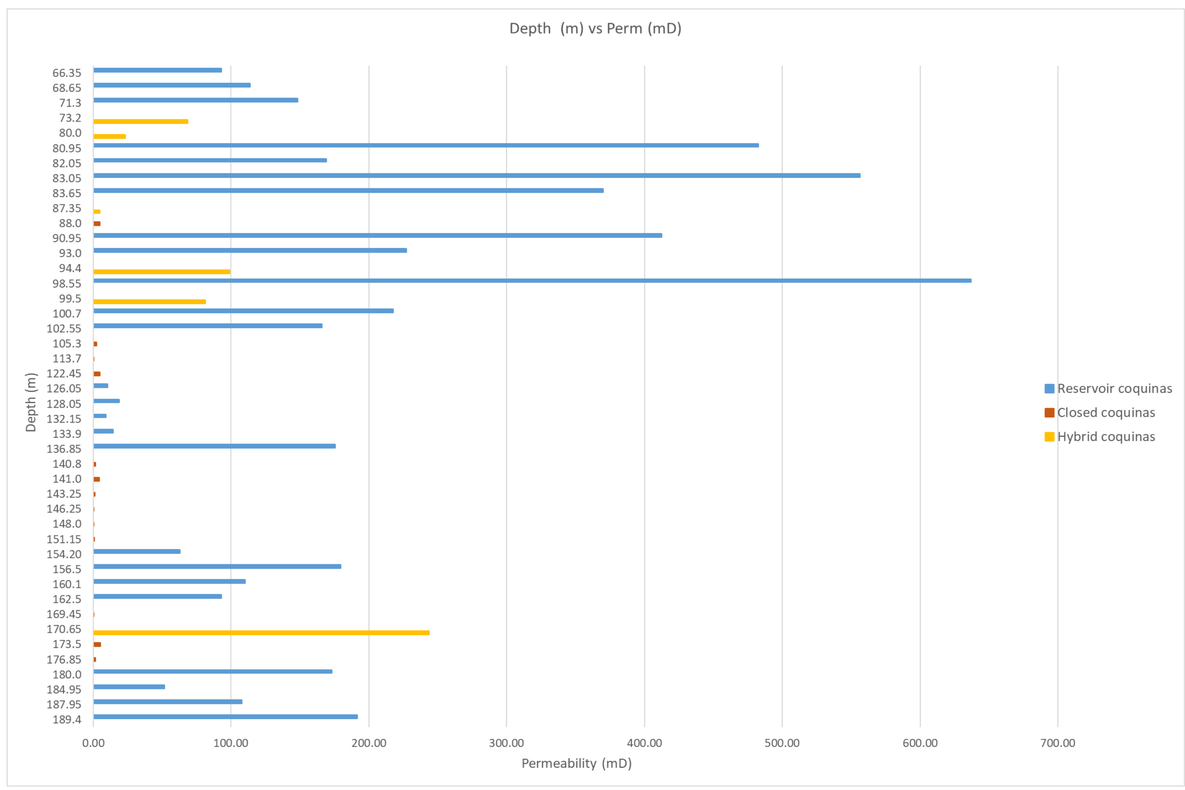

Distribution of Well Permeability in Depth by Rock Type

Table 3 – Correlation of the measured permeability compared to the permeability estimated using the Katz–Thompson equation for each rock type

Reservoir Coquinas	R^2	Closed Coquinas	R^2	Hybrid Coquinas	R^2
Perm x $r_{critNMR}$	0.29	Perm x $r_{critNMR}$	0.74	Perm x $r_{critNMR}$	0.78
Perm x $r_{critMICP}$	0.30	Perm x $r_{critMICP}$	0.79	Perm x $r_{critMICP}$	0.75
Perm x r_{critIP}	0.39	Perm x r_{critIP}	0.80	Perm x r_{critIP}	0.75

5. Future work

We plan to evaluate the permeability using critical radius for bimodal samples involving double porosity

6. References

Daigle, H. and Johnson, A. 2016. Combining Mercury Intrusion and Nuclear Magnetic Resonance Measurements Using Percolation Theory, Transport in Porous Media, 111:669–679, DOI 10.1007/s11242-015-0619-1.

Ghanbarian, B. and Skaggs, T. 2022. Soil water retention curve inflection point: Insight into soil structure from percolation theory. SOIL PHYSICS & HYDROLOGY NOTES, SSSA Journal. DOI: 10.1002/saj2.20360.

Lima-Santo, M. C. O. 2020. *Connectivity Study and its Influence on the Permeability Prediction in Carbonatic Rocks*. PhD Thesis. 152 pg. PEC/UFRJ. Rio de Janeiro.

This research was carried out in association with the ongoing R&D project registered as ANP nº 23020-1, "Análise Experimental da Recuperação Avançada de Petróleo em Reservatórios Carbonáticos do Pré-Sal do Brasil Através de Injeção Alternada de CO2 e Água – Fase II - Condições de Reservatório" (UFRJ/Shell Brasil/ANP), sponsored by Shell Brasil Petróleo Ltda under the ANP R&D levy as "Compromisso de Investimentos com Pesquisa e Desenvolvimento".

Transient Flow Effects on Solute Transport in an Unsaturated Soil

Luwen Zhuang[1], Yangkun Zheng[1], S.Majid Hassanizadeh[2], and Martinus Th. van Genuchten[2,3]

[1]School of Civil Engineering, Sun Yat-sen University, Zhuhai, P.R. China
[2]Department of Earth Sciences, Utrecht University, Utrecht, The Netherlands
[3]Department of Nuclear Engineering, Federal University of Rio de Janeiro, Rio De Janeiro, Brazil

Overview

The effects of the flow regime and soil saturation on solute transport processes can be significant, yet have not been adequately studied. To address this gap, we conducted a series of solute transport experiments in a sandy soil, complemented by numerical modeling, under both steady-state and transient flow conditions. Results from the steady-state experiments revealed a non-monotonic relationship between the dispersivity and saturation (first column below). Results for transient flow are in the second column. The fitted dispersivity–saturation function will be used in transient simulations. Analysis of the transient flow data is ongoing, with a special focus on the effects of dynamic capillarity.

Experimental Setup

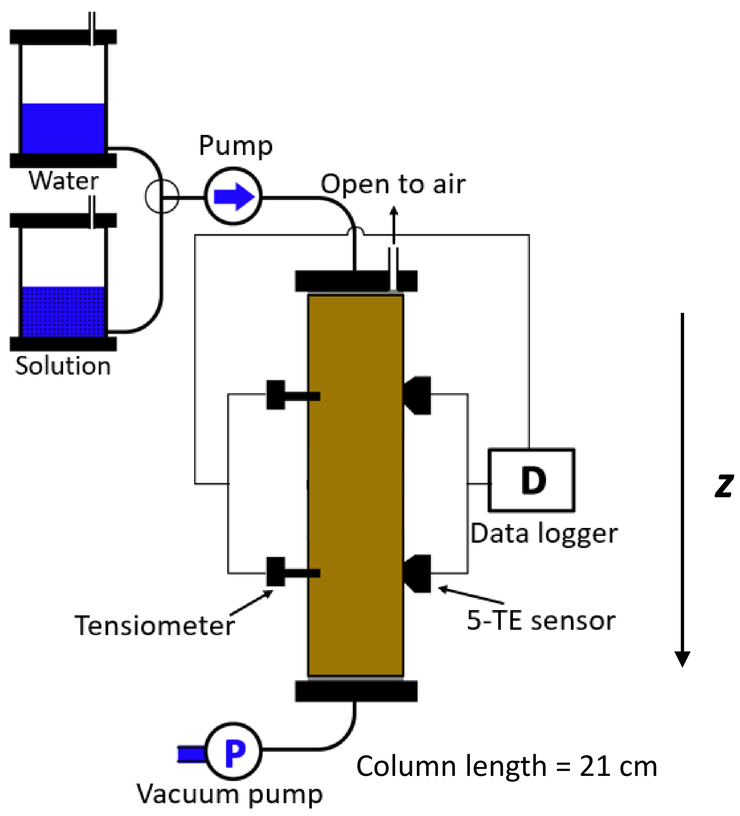

Results for Steady-State Flow Conditions

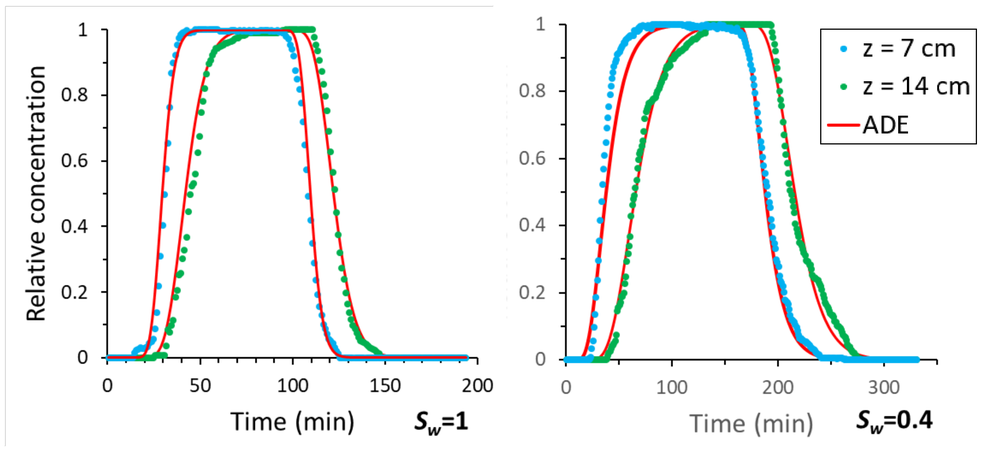

Dispersivity vs. Saturation

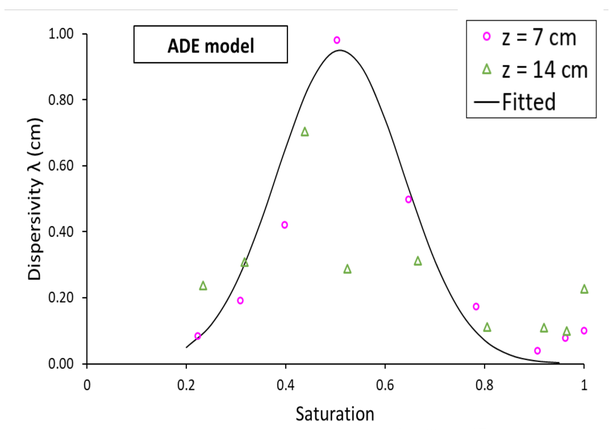

$$\lambda\left(S^w\right)=ae^{-\left(\frac{S^w-b}{c}\right)^2}$$

$a = 0.95$, $b = 0.51$, $c = 0.18$

Transient Flow Conditions

The soil column for the transient flow experiments was initially fully saturated without a tracer. The tracer solution was injected at the column's top while maintaining a constant pressure at the bottom using a hanging water column.

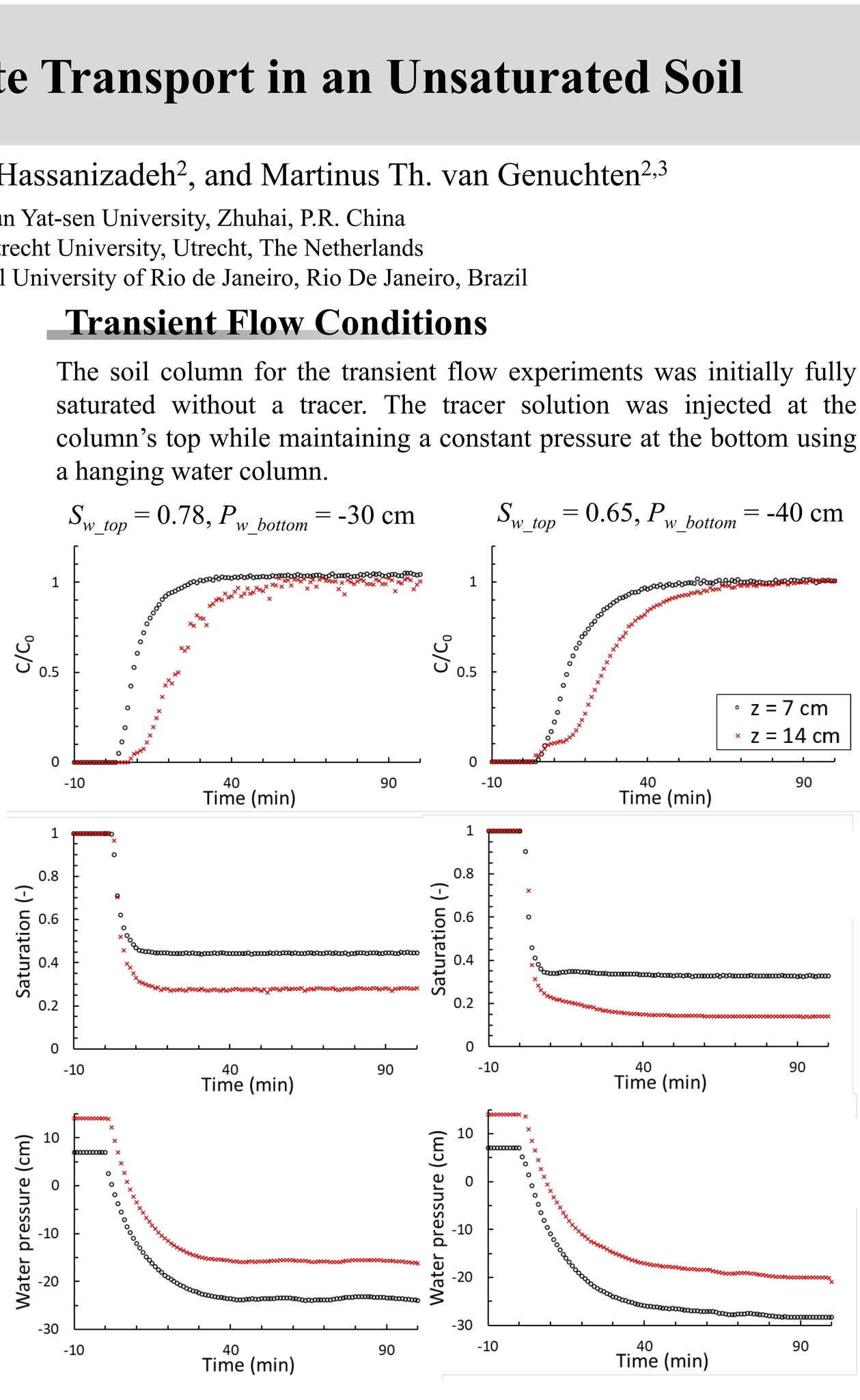

Governing Equations

$$\varphi\frac{\partial S^w}{\partial t}+\frac{\partial q}{\partial x}=0 \qquad q=-\frac{k^{rw}(S^w)k}{\mu^w}\left(\frac{\partial p^w}{\partial x}-\rho^w g\right)$$

$$-p^w=p^c(S^w)-\tau\frac{\partial S^w}{\partial t}$$

$$\frac{\partial S^w C}{\partial t}-\frac{\partial}{\partial x}\left(D\left(S^w,q\right)\frac{S^w C}{\partial x}\right)+\frac{\partial qC}{\varphi\partial x}=0$$

Ongoing Studies

- Numerical simulations will be carried out to investigate the simultaneous movement of water and solutes.
- The model will incorporate both constant and saturation-dependent dispersivities. Our analysis will focus primarily on the transient response.
- We will analyze the data also in terms of a dynamic capillary model.

References

Raoof, A.; Hassanizadeh, S.M. Saturation-dependent solute dispersivity in porous media: pore-scale processes. Water Resour. Res. 2013, 49 (4), 1943–1951.

Toride, N.; Inoue, M.; Leij, F. J. Hydrodynamic dispersion in an unsaturated dune sand. Soil Sci. Soc. Am. J. 2003, 67(3), 703–712.

Zhuang, L.; Raoof, A.; Mahmoodlu, M.G.; Biekart, S.; de Witte, R; Badi, L., van Genuchten, M.Th.; Lin, K. Unsaturated flow effects on solute transport in porous media, J. Hydrol. 2021, 598: 126301.

Zhuang, L.; Hassanizadeh, S.M.; Qin, C.-Z.; de Waal, A. Experimental investigation of hysteretic dynamic capillarity effect in unsaturated flow, Water Resour. Res. 2017, 53(11), 9078–9088.

Rien van Genuchten Conference
May 7-9, 2025
Rio de Janeiro, Brazil

COMPARISON OF NMR LOG T_2 DISTRIBUTIONS WITH PETROGRAPHIC IMAGE ANALYSIS AND SPECIAL CORE ANALYSIS IN THE PRE-SALT FORMATIONS OFFSHORE BRAZIL

Gabriel Ribeiro*, Austin Boyd, Maira Lima, Paulo Couto
LRAP⁺, Program of Civil Engineering, Federal University of Rio de Janeiro, Brazil

Introduction

Pre-salt carbonate reservoirs present major challenges for petrophysical interpretation due to their complex heterogeneity, mixed or oil-wet conditions, and the frequent use of synthetic oil-based mud (OBM) in drilling. These factors significantly affect NMR responses, often leading to bimodal T_2 distributions where OBM filtrate invades larger pores and water remains trapped in smaller ones. The key to interpreting this behavior is the surface relaxivity parameter (ρ), which links the T_2 signal to pore geometry. However, ρ is not constant and depends on mineralogy and pore structure, making its estimation critical for reliable NMR analysis. This study proposes an integrated workflow to estimate effective surface relaxivity and compare pore-size distributions (PSDs) derived from NMR logs and thin-section image analysis. The analysis was conducted using well data from 2A-ANP-RJS in the Mero Field, focusing on the Barra Velha and Itapema formations. This integration improves ρ estimation and helps us better understand pore structure and fluid distribution, supporting more reliable evaluation of carbonate reservoirs.

Methodology

This study proposes an integrated workflow to estimate the effective surface relaxivity parameter (ρ) and compare pore size distributions (PSDs) derived from NMR well logs and petrographic image analysis. We used data from well logs, routine core analysis, and 43 petrographic thin sections. Image segmentation allowed the extraction of morphological metrics of the pores, which were correlated with the T_2 distributions of NMR to estimate ρ. The methodological process followed the following steps:

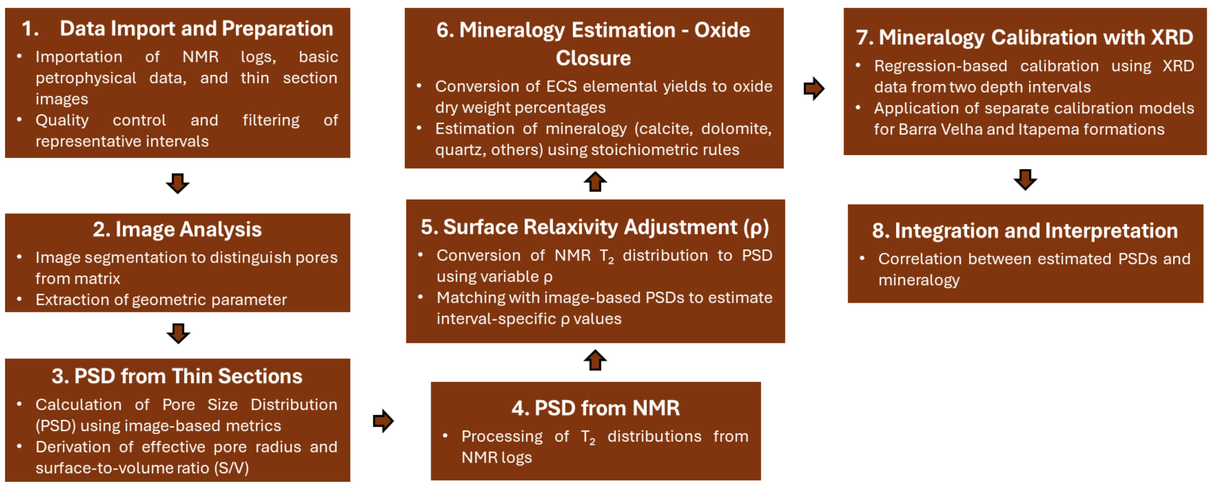

Figure 1: Workflow summarizing the steps from data processing to mineralogy and pore structure integration, supporting the surface relaxivity estimation and PSD comparison.

Results and Discussions

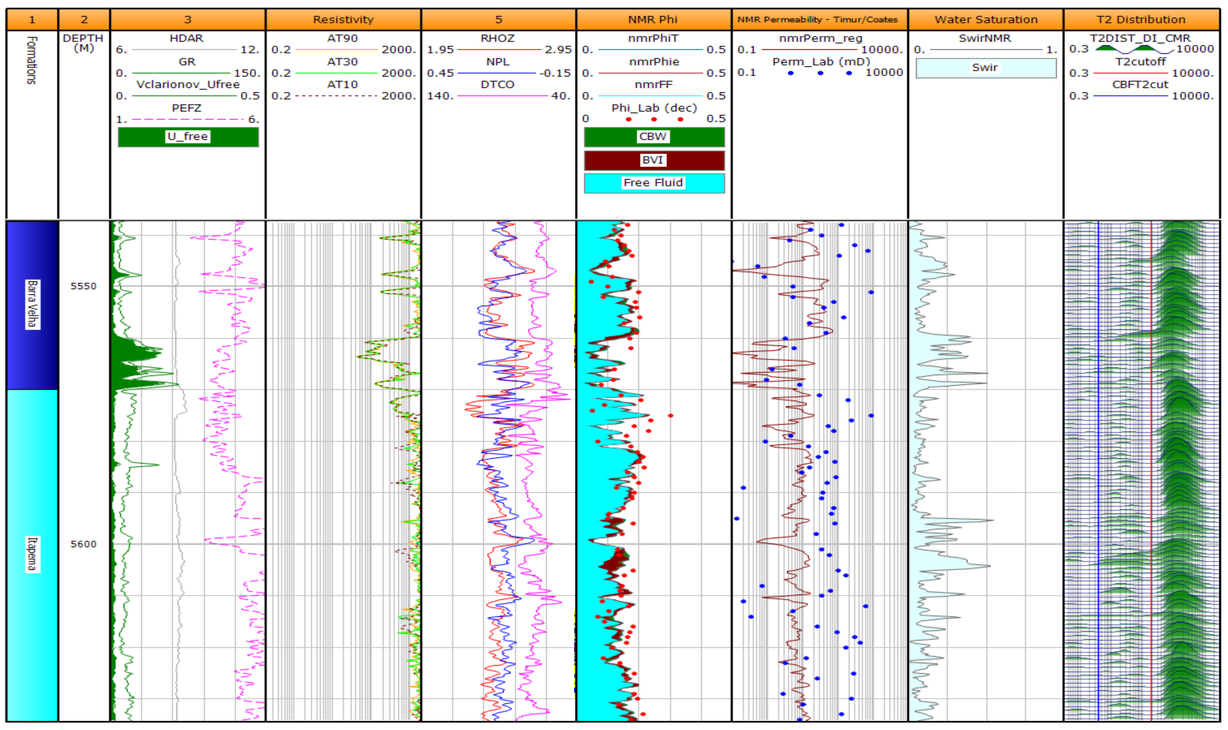

Figure 2: Log plot of the geophysical logs used in well 2-ANP-2A-RJS (Mero Field, Santos Basin).

Figure 2 shows a section of the Barra Velha and Itapema formations with the log plot of the main geophysical well logs used in this study. This section is located above the oil-water contact, which is situated in the Itapema Formation. In the T_2 distribution track, T_2 times in the Itapema Fm. are visually shifted to the right, suggesting the dominance of larger pores. The horizontal blue and red lines represent the conventional cutoffs of 3 ms (CBW) and 100 ms (BFM), used to separate bound water from the movable or free fluid fraction.

The porosity from NMR logs (nmrPhiT, nmrPhie, nmrFF) matches well with lab porosity (Phi_{Lab}), showing that NMR works well for porosity analysis in pre-salt carbonates. In contrast, the Timur-Coates model presents a weak visual correlation with core permeability, which is expected in highly heterogeneous carbonate systems. Table 1 highlights that the Barra Velha and Itapema formations exhibit similar average petrophysical properties, with the main difference being resistivity—likely influenced by fluid saturation and possible variations in pore connectivity or mineralogy.

Table 1: Statistics of petrophysical properties in the Barra Velha and Itapema formations.

Formations	Properties									
	GR (gAPI)	**Vclay_U$_{free}$** (%)	**AT90** (ohm.m)	**RHOZ** (g/cm³)	**NPL** (%)	**Phi$_{Lab}$** (%)	**nmrPhiT** (%)	**nmrPhie** (%)	**nmrFF** (%)	**nmrPerm** (mD)
Barra Velha	18.44	2.35	625.04	2.55	10.76	11.06	11.40	10.92	9.45	3.51
Itapema	14.95	1.33	64.06	2.49	11.29	15.13	11.43	10.95	9.41	2.59

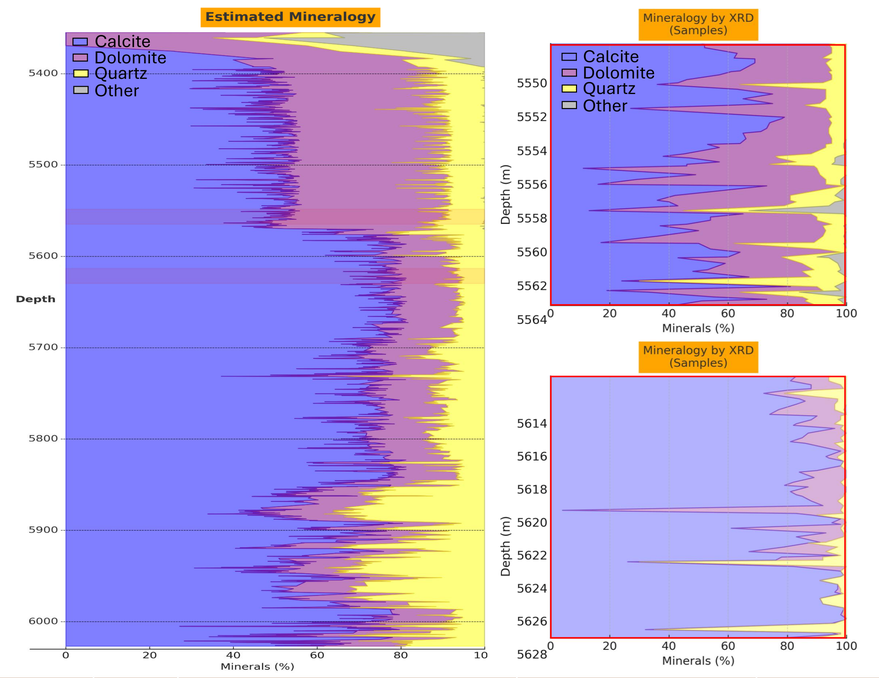

Formations	Minerals	XRD (%)	Oxide Closure with Regression (%)	Absolute Difference (%)	Relative Error (%)	ρ (μm/s)
Barra Velha	Calcite	51.94	49.86	-2.08	-4.01	22.0
	Dolomite	35.43	39.55	4.12	11.63	
	Quartz	10.83	10.57	-0.26	-2.40	
	Others	1.50	0.02	-1.48	-98.62	
Itapema	Calcite	85.54	75.95	-9.59	-11.21	81.5
	Dolomite	9.57	17.20	7.63	79.78	
	Quartz	4.86	6.85	1.99	40.83	
	Others	0.00	0.00	0.00	0.00	

Figure 3: Comparison between mineralogical logs estimated via Oxide Closure calibrated by linear regression and laboratory XRD data. The table summarizes the estimation errors and the mean ρ values calculated by fitting between image and NMR PSDs.

The mineralogical comparison reveals important textural differences between the Barra Velha and Itapema formations, directly impacting the surface relaxivity (ρ). Dolomite crystals in Barra Velha, typically smoother, contrast with the irregular calcite crystal structures in Itapema, increasing the surface area available for relaxation interactions. This interpretation aligns with literature, which indicates that calcite commonly exhibits more heterogeneous surfaces due to variable solubility and irregular precipitation, while dolomite tends to form smoother, uniform crystals (Lucia, 1995; Flügel, 2010). These textural features are reflected in the surface relaxivity adjustment (ρ = 25 μm/s for Barra Velha and ρ = 95 μm/s for Itapema), obtained by correlating the pore-size distributions from petrographic images with NMR data. This clearly shows how mineralogical heterogeneity significantly affects T_2 relaxation times, highlighting the need for formation-specific adjustments. Accounting for these variations enables more accurate petrophysical property estimates in highly complex carbonate reservoirs, such as those found in the Brazilian pre-salt.

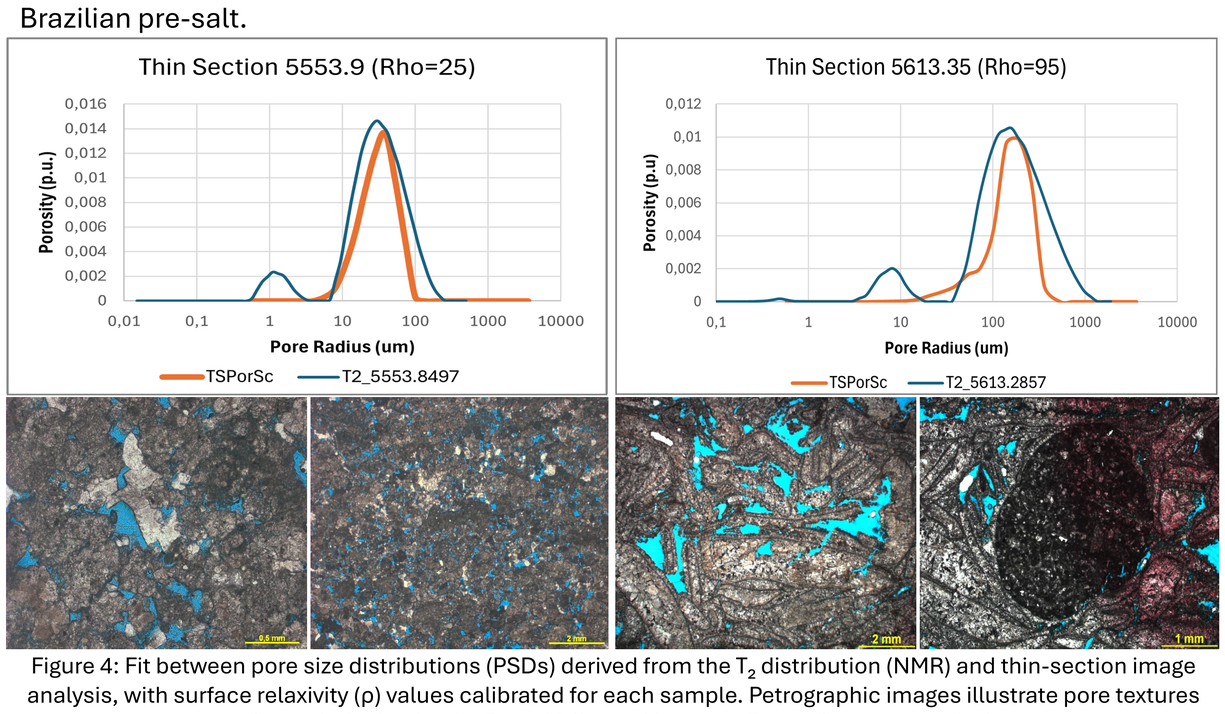

Figure 4: Fit between pore size distributions (PSDs) derived from the T_2 distribution (NMR) and thin-section image analysis, with surface relaxivity (ρ) values calibrated for each sample. Petrographic images illustrate pore textures and morphologies for the Barra Velha and Itapema Formations, respectively.

Future Work

Incorporate calibrated ρ values and integrated PSDs into predictive models for irreducible water saturation and permeability.

Acknowledgements

This research was carried out in association with the ongoing R&D project registered as ANP nº 23020-1, “Caracterização Experimental, Modelagem e Otimização de Processos de Injeção de Água Alternada Com Gás – WAG-EX Fase II" (UFRJ/Shell Brasil/ANP), sponsored by Shell Brasil Petróleo Ltda.

References

El-Husseiny, A. and Knight, R. “A Laboratory Study of the Link Between NMR Relaxation Data and Pore Size in Carbonate Skeletal Grains and Micrite” Petrophysics, 58(2), April 2017, pp. 116–125.
Flügel, E. Microfacies of Carbonate Rocks: Analysis, Interpretation and Application. 2nd Edition, Springer-Verlag, Berlin Heidelberg, 984 p, 2010.
Looyestijn, W. Practical Approach to Derive Wettability Index by NMR in Core Analysis Experiments, PETROPHYSICS, VOL. 60, NO. 4 (AUGUST 2019).
Lucia, F.J. Rock-Fabric/Petrophysical Classification of Carbonate Pore Space for Reservoir Characterization. AAPG Bulletin, 79(9), pp. 1275–1300, 1995.
Straley, C. Core Analysis by Low Field NMR, 1994 SCA Conference.
Ma, S.M. et al. “Objective Driven Solid Surface Roughness Characterization for Enhanced Formation Evaluation” SPE 201689-MS, presented at 2020 SPE ATC, October 26-29, Denver, Colorado.

Rien van Genuchten Conference
May 7-9, 2025
Rio de Janeiro, Brazil

Challenges and Opportunities in Porous Media Multiphase Flow and Contaminant Transport Research

Enhancing Relative Permeability Uncertainty Quantification via Sobol-Based Parameter Reduction in Unsteady-State Core Flooding

F. O. Silva[1]
E. S. Assis[2], G. M. Stieven[3], C. H. Dias[4], P. Couto[5].

Introduction

- Core-flooding experiments for fluid-flow behavior on porous media;
- Main Objective: Estimation of Relative Permeability (k_{rel}) curves;
- USS experiments: often requires solving an inverse problem to estimate multiple parameters which may lack physical meaning;
- This study employs Local Sensitivity Analysis (LSA) and Global Sensitivity Analysis (GSA) to evaluate influence of each parameter on Net Production (NP) and Differential Pressure (ΔP).

Methodology and Results

- Buckley-Leverett equation for one-dimensional, longitudinal multiphase (water/oil) flow, assuming incompressible fluids and constant water injection:

$$\phi\frac{\partial S_w}{\partial t}+v\frac{\mathrm{d}f_w}{\mathrm{d}S_w}\frac{\partial S_w}{\partial x}=0$$

- Parameterization of relative permeability via LET model:

$$S_{wn}=\frac{S_w-S_{wi}}{1-S_{wi}-S_{or}} \qquad k_{ro}=k_{ro}^{w}\frac{(1-S_{wn})^{L_o^w}}{(1-S_{wn})^{L_o^w}+E_o^w S_{wn}^{T_o^w}} \qquad k_{rw}=k_{rw}^{o}\frac{S_{wn}^{L_w^o}}{S_{wn}^{L_w^o}+E_w^o(1-S_{wn})^{T_w^o}}$$

- MCMC with Metropolis-Hasting acceptance Algorithm:

$$P(\mathbf{X}|\theta)=(2\pi)^{-\frac{N_{var}}{2}}|\mathbf{W}|^{-\frac{1}{2}}\exp\left\{-\frac{1}{2}\left[\mathbf{X}-\mathbf{Y}(\theta)\right]^{\top}\mathbf{W}^{-1}\left[\mathbf{X}-\mathbf{Y}(\theta)\right]\right\}$$

- LSA and GSA of all relative permeability parameters via Sobol:

$$\mathbf{J}=\frac{\partial\mathbf{Y}(\boldsymbol{\theta})}{\partial\boldsymbol{\theta}} \qquad \boldsymbol{S}=\frac{\mathrm{Var}_{\boldsymbol{\theta}}\left(\mathbb{E}[\boldsymbol{Y}|\boldsymbol{\theta}]\right)}{\mathrm{Var}(\boldsymbol{Y})}$$

Table 1: First order Sobol' indices for initial range of parameters.

	L_o	S_{or}	S_{wi}	E_o	k_{rw}	k_{ro}	T_o	T_w	L_w	E_w
ΔP	**0.10**	0.00	0.00	0.01	**0.14**	0.01	0.00	**0.09**	0.03	0.02
NP	**0.42**	**0.38**	0.05	0.03	0.02	0.02	0.01	0.01	0.01	0.00

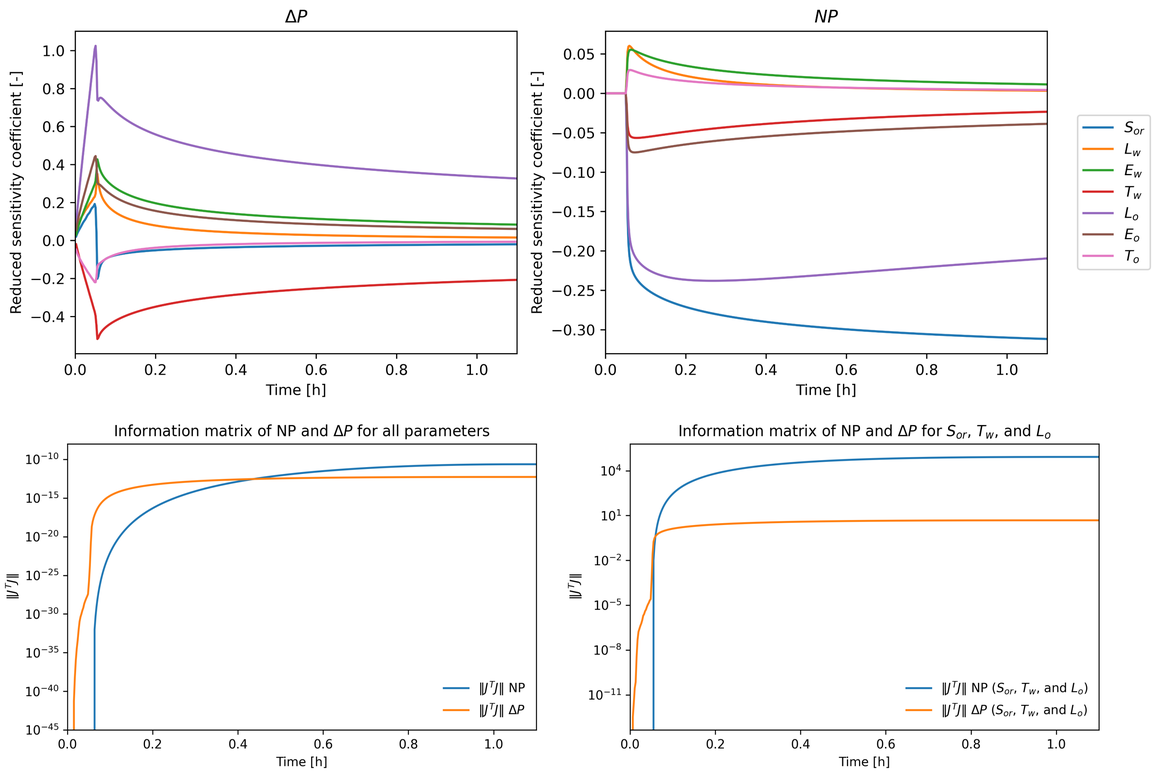

Fig. 1: Reduced sensitivity coefficients (top) and Information matrix (bottom) for relative permeability parameters (used on Case 2).

This research was carried out in association with the ongoing R&D project registered as ANP nº 24.551, "Avaliação de Metodologias para Interpretação de Curvas de Permeabilidade Relativa em meios porosos heterogêneos" (UFRJ/Petrobras Brasil/ANP), sponsored by Petróleo Brasileiro S/A under the ANP R&D levy as "Compromisso de Investimentos com Pesquisa e Desenvolvimento".

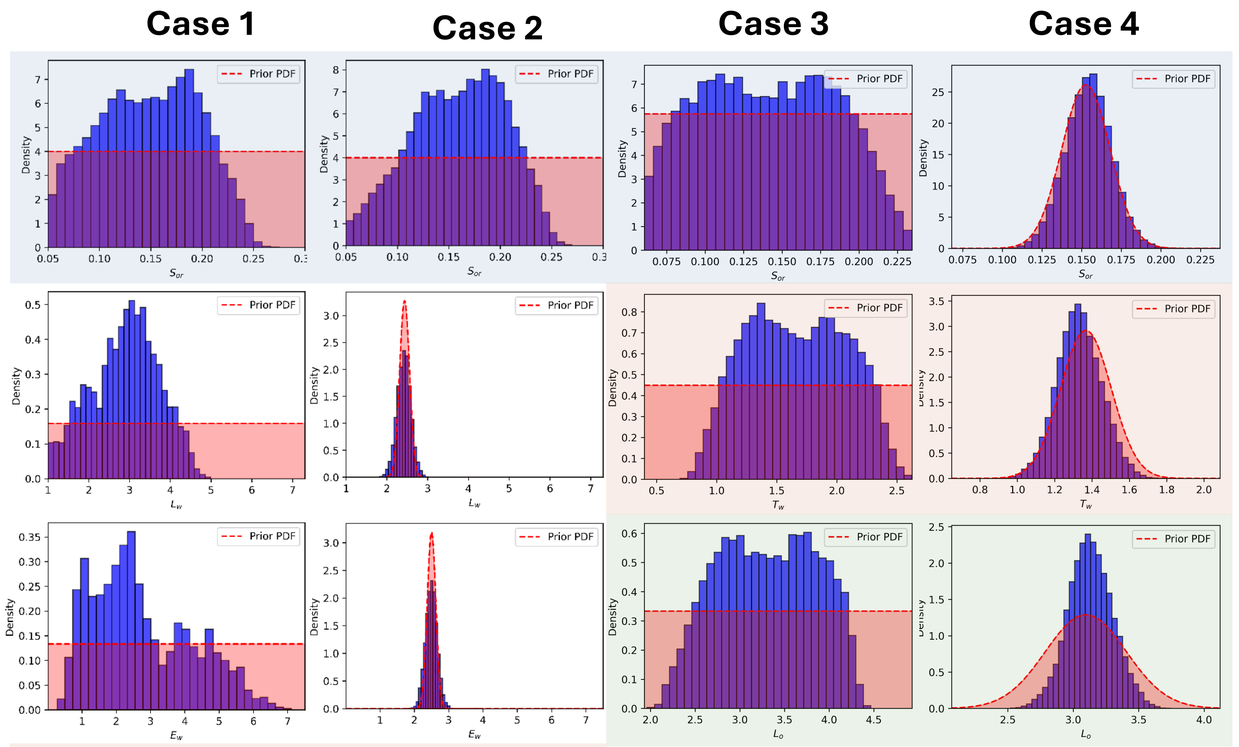

Fig. 2: MCMC results for cases 1 and 2.

Fig. 3: MCMC results for cases 3 and 4.

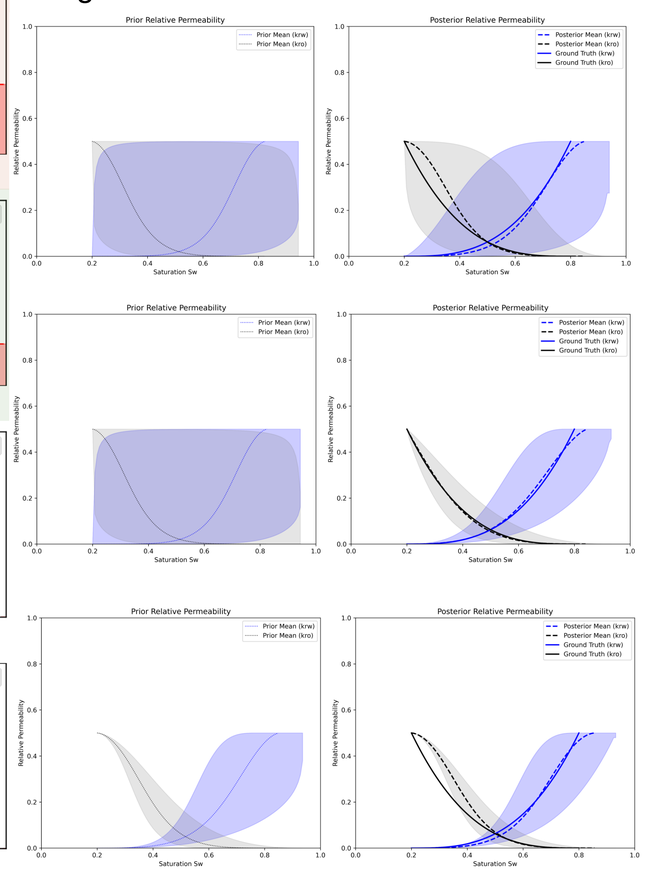

Fig. 4: k_{rel} curves for cases 1, 2, and 3.

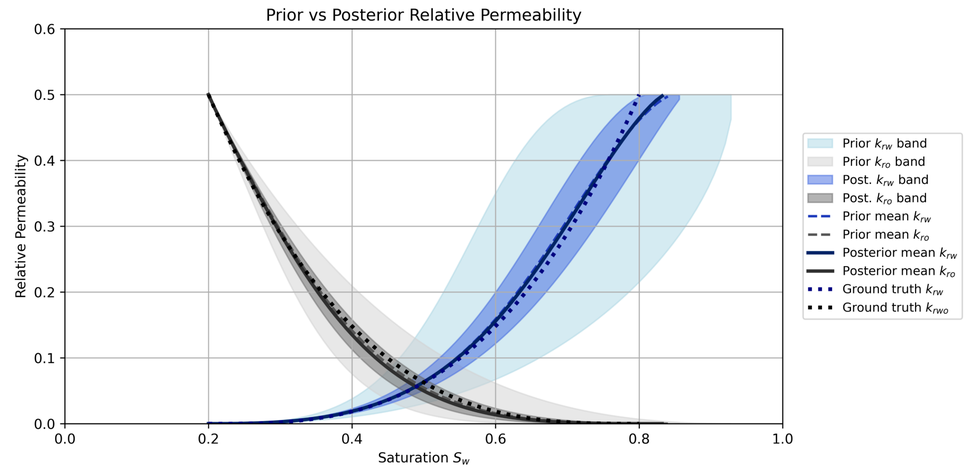

Fig. 5: Enhanced k_{rel} uncertainty quantification via LSA and GSA for case 4.

$$S_{wn}=\frac{S_w-0.2}{1-0.2-S_{or}} \qquad k_{ro}=\frac{1}{2}\frac{(1-S_{wn})^{L_o^w}}{(1-S_{wn})^{L_o^w}+2.465S_{wn}^{0.952}} \qquad k_{rw}=\frac{1}{2}\frac{S_{wn}^{2.415}}{S_{wn}^{2.415}+2.498(1-S_{wn})^{T_w^o}}$$

Conclusions

- Both LSA and GSA indicates hyperparameterization of the LET model;
- GSA and LSA proved useful in supporting decision-making regarding parameter reduction and uncertainty quantification.
- A detailed prior analysis may be a valuable approach for achieving more targeted parameter reduction.

Rien van Genuchten Conference
May 7-9, 2025
Rio de Janeiro, Brazil

Challenges and Opportunities in Porous Media Multiphase Flow and Contaminant Transport Research

Assessment of Experimental Uncertainty Impact on Capillary Pressure Determination via the Centrifuge Technique

Felipe M. Eler[1], Paulo Couto[2]
1. Ph.D. Candidate at PEC/COPPE/UFRJ felipe.eler@petroleo.ufrj.br 2. Professor at PEC/COPPE/UFRJ

Introduction

Since Hassler and Brunner (1945) introduced the centrifuge as an alternative to capillary pressure measurement, the technique has evolved and become more popular. Centrifuge has been used to determine the first drainage curve (McPhee et al., 2015), the imbibition curve for coreflooding support (Berg et al., 2021; Maas et al., 2019), and the USBM wettability index (Anderson, 1986).

The centrifuge technique is known for its necessity of inversion from average to inlet face saturations (Forbes, 1994). Eq.1 shows the relationship between average ($\overline{S_w}$) and local (S_w) water saturation for the first drainage case.

$$\overline{S_w} = \frac{1}{(r_2 - r_1)} \int_{r_1}^{r_2} S_w(r)\,dr \qquad \text{Eq. 1}$$

where $\overline{S_w}$ is the average water saturation, r_1 and r_2 are the distances from the axis of rotation and the sample ends (see Figure 1), and $S_w(r)$ is the local saturation, a function of position r.

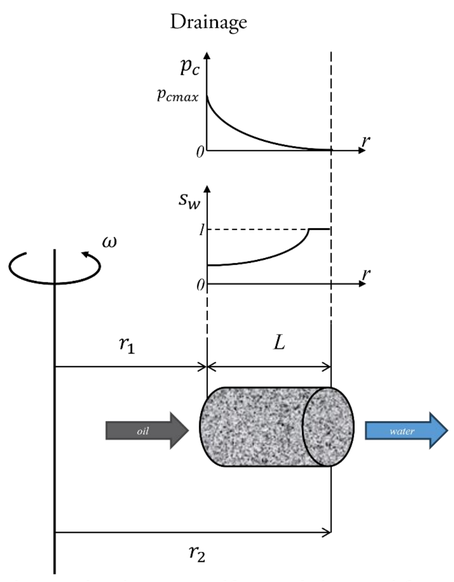

Figure 1. Schematics of drainage in the centrifuge. Adapted from Albuquerque et al. (2018)

Methodology and Results

In the present work, an inverse approach using Van Genuchten's equation (1980) was used to access the technique's sensibility to experimental noise. In this approach, Equation 1 was modified to left S_w as a function of P_c (Equations 2 and 3), and Van Genuchten's equation was written in the following format:

$$\overline{S_w}(p_{cmax}) = \frac{1 + \sqrt{1 - B}}{2} \int_0^1 \frac{S_w(x p_{cmax})}{\sqrt{1 - Bx}}\,dx \qquad \text{Eq. 2}$$

$$B = 1 - \left(\frac{r_1}{r_2}\right)^2 \qquad \text{Eq. 3}$$

$$\frac{S_w - S_{wi}}{1 - S_{wi}} = \left[\frac{1}{1 + (\alpha P_c)^n}\right]^m \qquad \text{Eq. 4}$$

Aiming to control the ground truth solution, synthetic data was used to evaluate the noise level's impact on the local saturation recovery. The noise levels introduced in the centrifuge's volume readings were 0.05, 0.10, 0.25, and 0.50 cm^3. This range covers automated centrifuge readings (0.05-0.10) to operator visual readings (0.25 - 0.50 cm^3).

The local saturations were recovered using the Markov Chain Monte Carlo method. The posterior distribution of the parameters was used to assess the uncertainty and determine the 95% confidence interval. We also compared the use of uninformative and informative priors in recovering the ground truth data. Figure 2 presents the recovered P_c curves for the different error levels using uninformative priors. Figure 3 presents a comparison between uninformative and informative priors for the 0.25 cm^3 case.

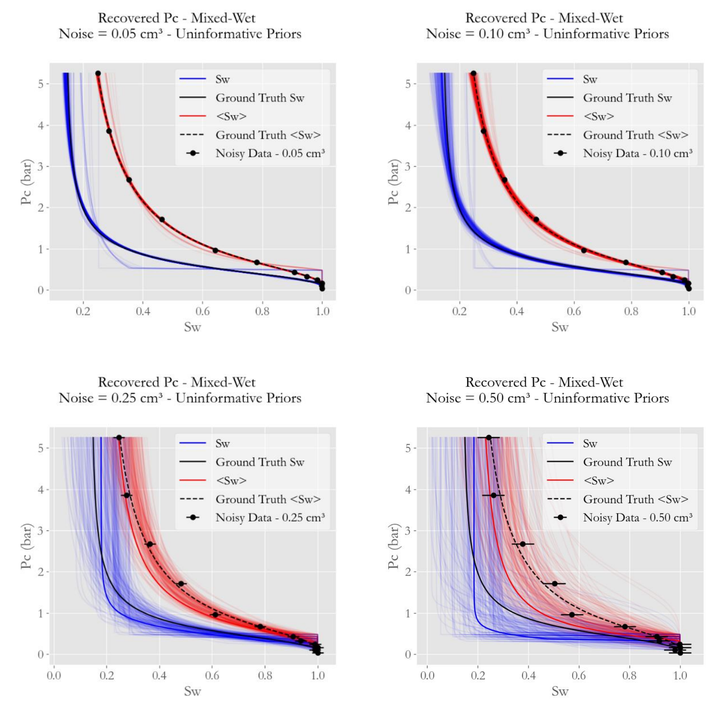

Figure 2. Recovered P_c curves for the different error levels using uninformative priors.

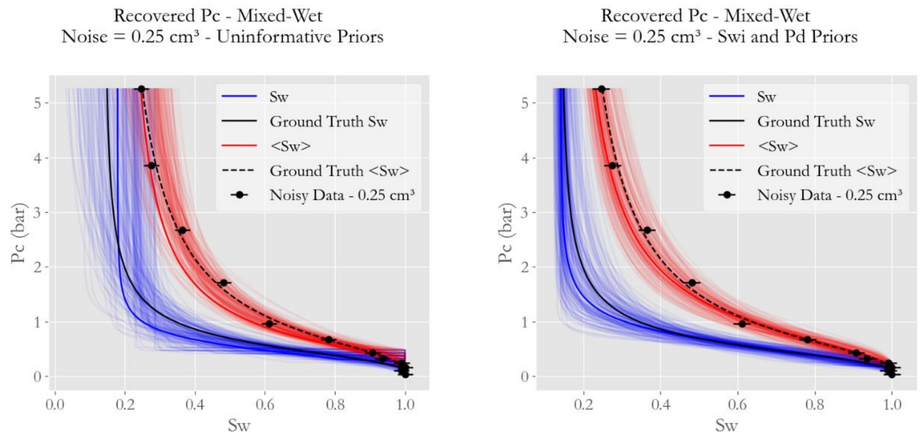

Figure 3. Comparison between the use of uninformative and informative priors for the noise level of 0.25 cm^3.

Conclusions

From Figure 2, it is possible to conclude that the increase in noise makes the predictions more uncertain and that only the low errors (0.05 and 0.10 cm^3) result in usable curves. From Figure 3, we conclude that prior knowledge of S_{wi} and P_d can significantly reduce the uncertainty and improve the accuracy of the estimates. The proposed technique using the Van Genuchten equation and MCMC proved to reliably recover the P_c curve for noise levels up to 0.25 cm^3 when informative priors are used.

This research was carried out in association with the ongoing R&D project registered as ANP nº 23020-1, "Análise Experimental da Recuperação Avançada de Petróleo em Reservatórios Carbonáticos do Pré-Sal do Brasil Através de Injeção Alternada de CO2 e Água – Fase II - Condições de Reservatório" (UFRJ/Shell Brasil/ANP), sponsored by Shell Brasil Petróleo Ltda under the ANP R&D levy as "Compromisso de Investimentos com Pesquisa e Desenvolvimento".

Integral Transform Solution for the Three-dimensional Modeling of Aquifer Drawdown and Recovery by Multiple Wells

Elizeu Melo da Silva[a](Speaker), João N. N. Quaresma[b], Emanuel N. Macêdo[b], Renato M. Cotta[d,e]

•[a] School of Mining Engineering, UNIFESSPA, Universidade Federal do Sul e Sudeste do Pará, Marabá, PA, Brazil
•[b] Graduate Program in Natural Resource Engineering in the Amazon, PRODERNA/ITEC/UFPA, Universidade Federal do Pará, Belém, PA, Brazil
•[c] School of Chemical Engineering, FEQ/ITEC/UFPA, Universidade Federal do Pará, Belém, PA, Brazil
•[d]IPqM/CTMRJ, General Directorate of Nuclear and Technological Development, DGDNTM, Brazilian Navy, Rio de Janeiro, RJ, Brazil
•[e] Department of Mechanical Engineering, POLI & COPPE, CT, Universidade Federal do Rio de Janeiro, Rio de Janeiro, RJ, Brazil

$$\theta(h) = \theta_r + \frac{\theta_s - \theta_r}{[1+|\alpha h|^n]^m}$$

Rien van Genuchten Conference

Introdução

Analytical solutions are essential tools for modeling aquifer drawdown and recovery, as they provide closed-form expressions that enable fast and efficient evaluations. This study presents an analytical 3D solution for groundwater flow induced by multiple vertical wells and radial collector wells. The model addresses both drawdown and recovery phases, allowing comparison with benchmark solutions.

Mathematical Modeling

The dimensionless model that describes the three-dimensional pressure distribution h(x,y,z,t) varying in the direction of the sinks located at points ($x_{0,i}$, $y_{0,i}$ (in Vertical Multiwells (VMw) or Radial Collector Multiwells (RCMw) is expressed as:

$$\frac{\partial h}{\partial t} = \frac{\partial^2 h}{\partial x^2} + k_y \frac{\partial^2 h}{\partial y^2} + k_z \frac{\partial^2 h}{\partial z^2} + q_i(x,y,z) \therefore 0<x<w_x;\ 0<y<w_y;\ -1<z<0 \text{ e } 0<t \quad (1.a)$$

$$h(x,y,z,0) = h_0(x,y,z) \quad (1.b)$$

$$\frac{\partial h(0,y,z,t)}{\partial x} - k_1 h(0,y,z,t) = 0;\quad \frac{\partial h(w_x,y,z,t)}{\partial x} + k_2 h(w_x,y,z,t) = 0 \quad (1.c\text{-}d)$$

$$\frac{\partial h(x,0,z,t)}{\partial y} = 0;\quad \frac{\partial h(x,w_y,z,t)}{\partial y} = 0 \quad (1.e\text{-}f)$$

$$\frac{\partial h(x,y,-1,t)}{\partial z} = 0\ ;\quad \frac{\partial h(x,y,0,t)}{\partial z} + k' h(x,y,0,t) + \frac{\sigma}{k_z}\frac{\partial h(x,y,0,t)}{\partial t} = 0 \quad (1.g\text{-}h)$$

where

$$q_i(x,y,z,Q_i) = \begin{cases} \sum_{i=1}^{Nw} Q_i \delta(x-\bar{x}_{0,i})\delta(y-\bar{y}_{0,i}) & \text{to VMw} \\ \sum_{i=1}^{Nw} Q_i \delta(x-\bar{x}_{0,i})\delta(y-\bar{y}_{0,i})\delta(z+\bar{z}_0) & \text{to RCMw} \end{cases} \quad (1.i)$$

The source term q_i defines the well at point ($x_{0,i}$, $y_{0,i}$) with constant pumping rate Q_i, i=1,2,3…,N_w, where N_w is wells number, as shown in Fig. 1.a for RCMw and Fig. 1.b for VMw.

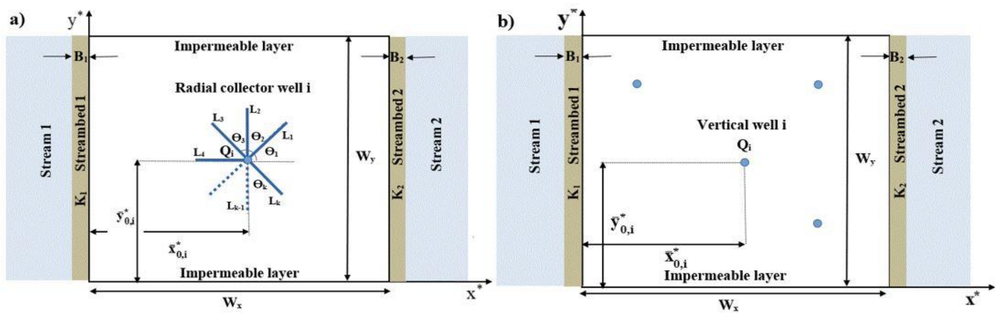

Figure 1-Horizontal and Vertical wells distribution: (a) Horizontal; (b) Vertical

Methodology – Classical Integral Transform Technique (CITT)

1. Filter the governing equation;
2. Auxiliary filter problem solution;
3. Application of the Integral Transform to reduce the PDE to an ODE.
4. Solution of the transformed equation using classical methods.
5. Inverse transform to recover the physical solution.

After filtering Equation 1 we obtain a particular auxiliary problem, $h_f(x,y,z)$, and a purely homogeneous problem, $h_H(x,y,z)$. The particular problem is solved by separation of variables while the homogeneous problem is solved by CITT, integrating the equations obtained multiplied by the eigenfunctions over the volume, we obtain the following decoupled infinite transformed system of first-order homogeneous ODEs, together with their initial conditions:

$$\frac{d\bar{h}_{m,p,r}(t)}{dt} + \mu^2_{m,p,r}\bar{h}_{m,p,r}(t) = 0 \quad (2.a)$$

$$\bar{h}_{m,p,r}(0) = \bar{f}_{m,p,r} \quad (2.b)$$

where:

$$\bar{f}_{m,p,r} = \int_0^{w_x}\int_0^{w_y}\int_{-1}^{0} \Psi_{m,p,r}(x,y,z)F(x,y,z)dzdydx + \sigma\int_0^{w_x}\int_0^{w_y}\Psi_{m,p,r}(x,y,0)F(x,y,0)dydx \quad (2.c)$$

$$F(x,y,z) = h_0(x,y,z) - h_f(x,y,z) \quad (2.d)$$

The Equations (2) have a purely analytical solution given by

$$\bar{h}_{n,p,r}(t) = f_{n,p,r}e^{-\mu^2_{n,p,r}t} \quad (3)$$

Therefore, by introducing Eq. (3) into the inverse formula, the solution for the problem is then obtained:

$$h(x,y,z,t) = \sum_{n=1}^{nt}\sum_{p=0}^{nt}\frac{\Psi_{n,p,0}(x,y,z)}{\bar{N}_{n,p,0}}\bar{h}_{n,p,0}(t) + \sum_{n=1}^{nt}\sum_{p=0}^{nt}\sum_{r=1}^{nt}\frac{\Psi_{n,p,r}(x,y,z)}{\bar{N}_{n,p,r}}\bar{h}_{n,p,r}(t) + \sum_{n=1}^{mt}\sum_{p=0}^{mt}\frac{\phi_{n,p}(x,y)}{\bar{N}_{n,p}}\tilde{\bar{Z}}_{n,p}(z) \quad (4)$$

on what $\Psi_{n,p,r}(x,y,z) = X_n(x)Y_p(y)Z_{n,p,r}(z)$ is the product of eigenfunctions in the x, y, z directions, while $\mu^2_{n,p,r}=\alpha^2_n+\beta^2_p+\delta^2_{n,p,r}$ is the sum of the squares of the respective eigenvalues for each eigenfunction. Yet, $\phi_{n,p}(x,y)=X_n(x)Y_p(y)$ is the product of eigenfunctions in the x and y directions and $\lambda^2_{n,p}=\alpha^2_n+\beta^2_p$ is the sum of the squares of their respective eigenvalues. N_n, N_p e $N_{n,p,r}$ are the norms in the respective x, y, and z directions. $\tilde{\bar{Z}}_{n,p}(z)$ is obtained from the solution of the problem:

$$k_z\frac{d^2\tilde{\bar{Z}}_{n,p}(z)}{dz^2} - \lambda^2_{n,p}\tilde{\bar{Z}}_{n,p}(z) = \tilde{\bar{P}}_{n,p}(z)$$

$$\frac{d\tilde{\bar{Z}}_{n,p}(0)}{dz} + k'\tilde{\bar{Z}}_{n,p}(0) = 0,$$

$$\frac{d\tilde{\bar{Z}}_{n,p}(-1)}{dz} = 0$$

where:

$$\tilde{\bar{P}}_{n,p}(z) = \begin{cases} \tilde{\bar{P}}_{V_{n,p}} = \bar{q}_{n,p}, \text{ if MVw} \\ \tilde{\bar{P}}_{H_{n,p}} = \bar{q}_{n,p}\delta(z+\bar{z}_0), \text{ if MCRw} \end{cases}$$

$$\bar{q}_{n,p} = \sum_{i=1}^{N_w} Q_i \tilde{\bar{G}}_{n,p}(\bar{x}_{0,i},\bar{y}_{0,i})$$

$$\tilde{\bar{G}}_{n,p}(\bar{x}_{0,i},\bar{y}_{0,i}) = \int_0^{w_x}\int_0^{w_y} X_n(x)Y_p(y)\delta(x-\bar{x}_{0,i})\delta(y-\bar{y}_{0,i})dydx = X_n(\bar{x}_{0,i})Y_p(\bar{y}_{0,i})$$

This procedure simplifies the solution of 3D problems involving complex well geometries. The transform solution is implemented in Wolfram Mathematica®.

Verification and Results

The proposed solution is verified against benchmark cases for:

- Single vertical wells
- Multiple vertical wells
- Radial collector wells (horizontal laterals)

Graphs show excellent agreement, Figs. 2 and 3, with known solutions, confirming the validity of the transform-based method. The solution was implemented in Wolfram Mathematica (Wolfram, 2015) for the calculation of eigenvalues and reordering of the involved summations. The parameters used are those in Table 1 below.

Table 1: Dimensional and dimensionless input parameters.

Dimensional	Value	Unit	Dimensionless	Value
S_y, S_s	0.3, 10^{-4}	m^{-1}	σ	150
K_x, K_y, K_z	1, 1, 0.01	m/day	k_y, k_z	1, 2.25
W_x, W_y, H	10^3, 10^3, 20	m	w_x, w_y	10/3,10/3
K', B	0, 1	m/day, m	k'	0
K_1, B_1	1, 1	m/day, m	k_1	300
K_2, B_2	0, 1	m/day, m	k_2	0
$(x^*_{0,i}, y^*_{0,i}, -z^*_0)$	-	m	$(x_{0,i}, y_{0,i}, -z_0)$	-
x^*_0	$x^*_{0,1}$	m	-	-
L^*_k	100	m	L_k	1/3
Q^*_i	-	m^3/day	Q_i	-
Q_0	$\lvert Q^*_1\rvert$	m^3/day	-	-

4.1. Solution verification

To perform the verification of the present solution, comparisons will be made with different cases available in the literature, namely, in three different scenarios involving vertical wells, horizontal wells, and multiple vertical and/or horizontal wells in PAT problems.

4.1.1. Vertical wells

The present solution is first verified by comparing it to the results obtained by Silva et al. (2021), Fig 2, who applied the Generalized Integral Transform Technique (GITT) to the problem proposed by Huang et al. (2014).

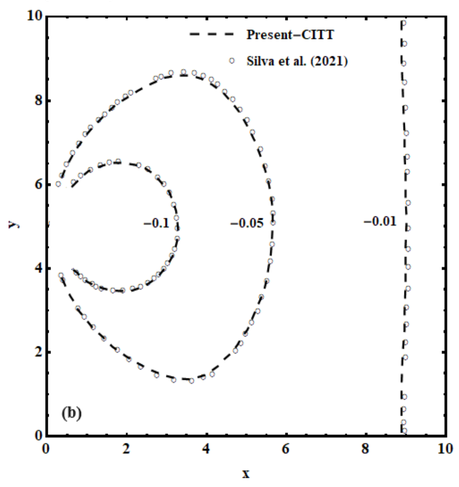

Fig. 2. Comparisons of the solution in Silva et al. (2021), Huang et al. (2014), and the present integral transform-solution: Pressure head h(x,y,0,10^5) distribution near the vertical well Eq. (22).

4.1.2. Horizontal wells

In the next analysis, the behavior of the methodology when applied to problems involving horizontal collector wells was analyzed. Eqs. (22) and (24.b) were computed as applied to the problem described by Huang et al. (2016), who studied the influence of collector wells in an unconfined aquifer, K'=0, with dimensions W_x=W_y=400 m and depth H=20 m, located at the position $(x^*_{0,1}, y^*_{0,1}, -z^*_0)$=(200, 200, -10). The simulation results are presented in Fig. 3 below, demonstrating an excellent agreement between the two independent approaches.

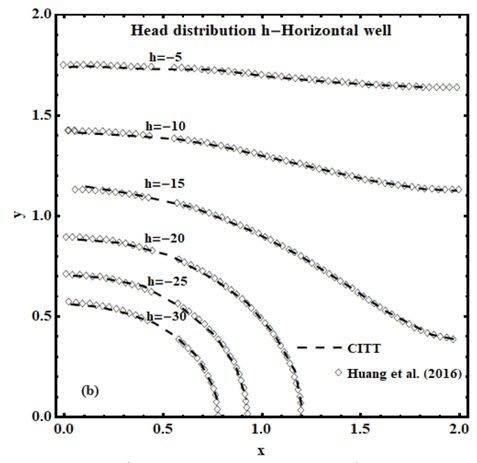

Fig. 3. Comparisons of the present integral transform solution with Huang et al. (2016) for Eq. (22) Head distribution near the horizontal well.

4.1.3. Effect of number and type of wells

For this purpose, the behavior of the solution is examined when applied to a case involving four wells with different flow rates, Q^*_i={-25,-25,-25,100} m^3/s, i.e., N_w=4 and Q_0=25, located at coordinates $(x^*_{0,1}, y^*_{0,1}) = (300,300)$; $(x^*_{0,2}, y^*_{0,2}) = (300,700)$; $(x^*_{0,3}, y^*_{0,3}) = (700,300)$ and $(x^*_{0,4}, y^*_{0,4}) = (700,700)$, at a fixed depth z^*_0=10. The aquifers have widths W_x=W_y=1000 m and depth H=20 m, bordered by a river with a semi-permeable bed of conductivity K_1=1 m/day at x^*=0 and isolated at x^*=W_x, K_2=0. The aquifer is isolated at the y^* boundaries. Each well has four collectors L^*_k=100 m, oriented at angles: Θ_1=0, Θ_2= π/2; Θ_3= π, Θ_4=3π/2, i.e., N_k=4This case simulates a PAT problem of recovering aquifers near a river, and the results can be observed in Fig 4.

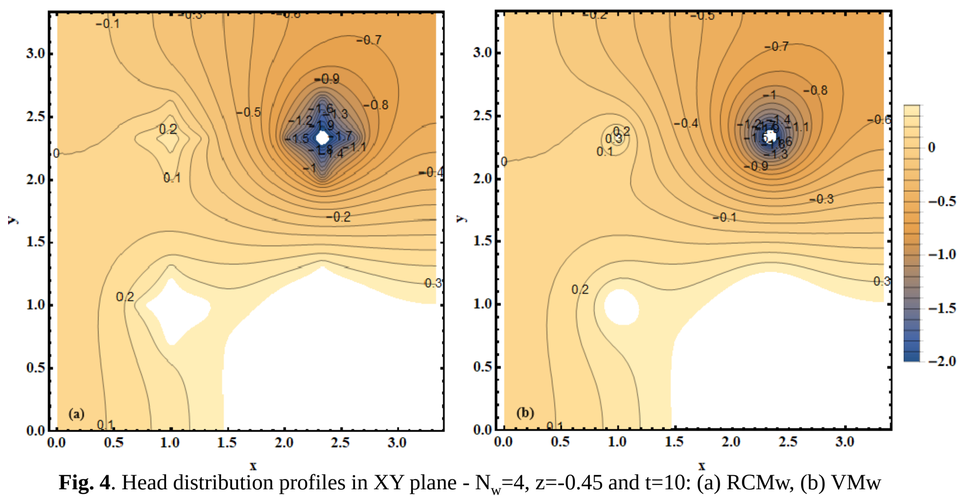

Fig. 4. Head distribution profiles in XY plane - N_w=4, z=-0.45 and t=10: (a) RCMw, (b) VMw

Conclusions

The proposed analytical approach demonstrates strong potential for accurately modeling 3D aquifer drawdown and recovery due to multiple well configurations. The use of the Classical Integral Transform Technique yields closed-form, efficient solutions for scenarios involving vertical and radial wells. This method is especially useful for rapid assessments.

References

Cotta, R.M., Mikhailov, M.D., 1997. Heat Conduction: Lumped Analysis, Integral Transforms, Symbolic Computation. J. Wiley & Sons.
Mikhailov, M.D., Özisik, M.N., 1984. Unified Analysis and Solutions of Heat and Mass Diffusion. John Wiley, New York.
Huang, C.S., Lin, W.S, Yeh, H.D., 2014. Stream filtration induced by pumping in a confined, unconfined or leaky aquifer bounded by two parallel streams or by a stream and an impervious stratum. Journal of Hydrology 513, 28-44, DOI:10.1016/j.jhydrol.2014.03.039
Huang, C.S., Chen, Y.L., Yeh, H.D., 2016. Approximate analysis of three-dimensional groundwater flow toward a radial collector well in a finite-extent unconfined aquifer. Hydrol. Earth Syst. Sci., 20, 55–71, https://doi.org/10.5194/hess-20-55-2016.
Özisik, M.N., 1980. Heat Conduction. John Wiley & Sons, Inc., Hoboken, New York. ISBN: 9780471054818, 978-0471054818.
Silva, E.M., Quaresma, J. N. N., Macêdo, E.N., Cotta, R.M. Integral transforms for three-dimensional pumping in confined, leaky, and unconfined aquifers. J. Hydrol. Hydromech., 69, 2021, 3, 319–331. DOI: 10.2478/johh-2021-0020. ISSN 1338-4333.

Rien van Genuchten Conference
May 7-9, 2025
Rio de Janeiro, Brazil

Challenges and Opportunities in Porous Media Multiphase Flow and Contaminant Transport Research

Influence of Inlet-End Diffusers Under Heterogeneous Conditions in 3D SCAL Models

C. H. Dias[1]
D. S. Almeida[2], F. O. Silva[3], G. M. Stieven[4], P. Couto[5].

Introduction

- Core flooding tests help determine reservoir properties but often overlook the impact of inlet diffusers on flow, especially in heterogeneous rocks;
- This study uses 3D unsteady-state CMG® IMEX simulations to show that inlet diffuser geometry strongly influences saturation, pressure drop, and oil recovery, which can impact SCAL reliability and property estimation.

Methodology and Results

- **Simulations in CMG® IMEX (Black-Oil model)** modeled unsteady-state core flooding;
- **Six diffuser geometries** were tested: homogeneous, central point, half-moon, star, spiral, and concentric;
- **Three rock scenarios** analyzed: homogeneous core, laminated heterogeneity, and vugular heterogeneity.

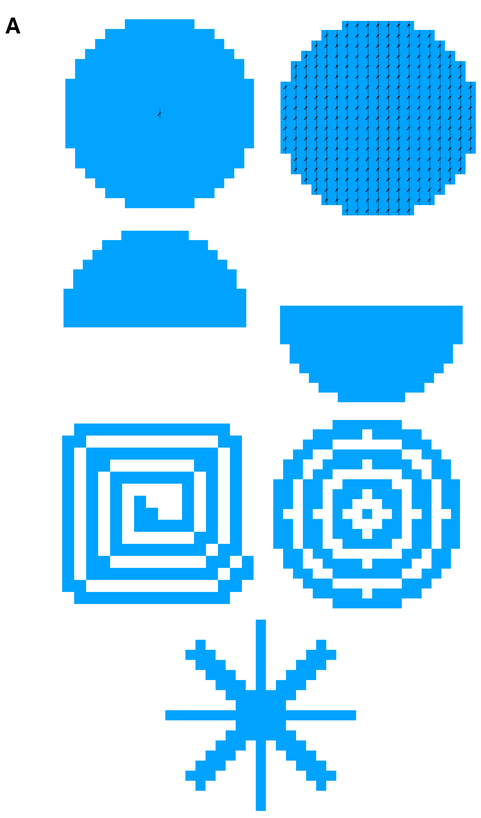

Fig. 1: A. Schematic of the modeled headers; B. Schematic of the heterogeneities modeled for simulation.

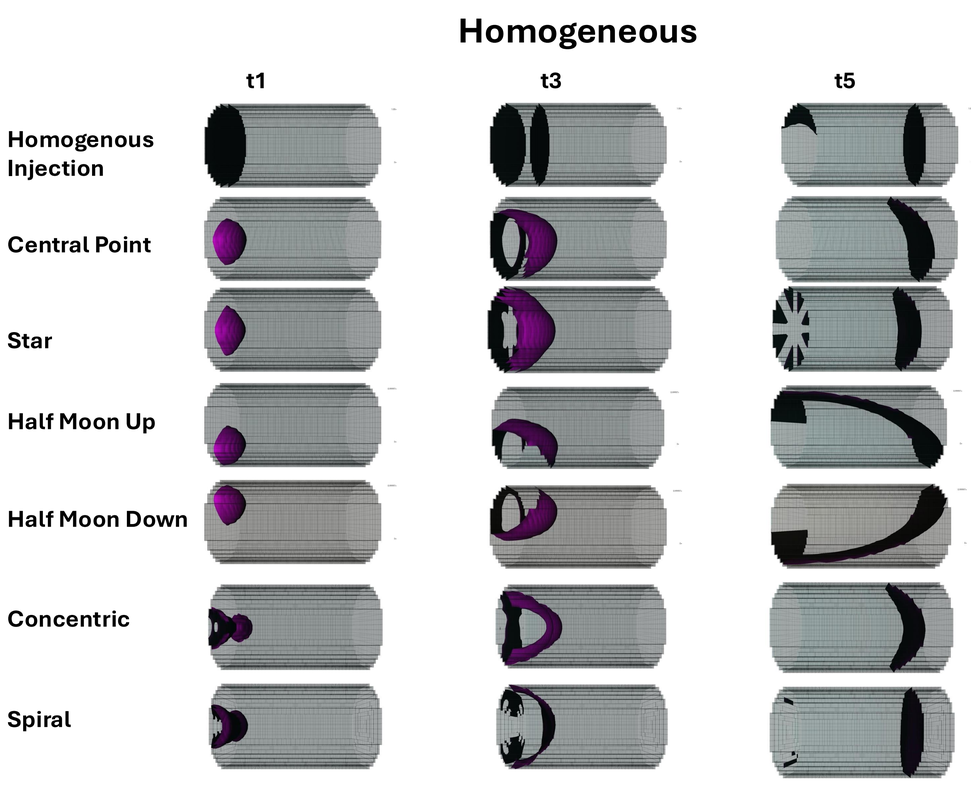

Fig. 2: Water saturation frontal advance with Sw = 0.21 for homogeneous scenario.

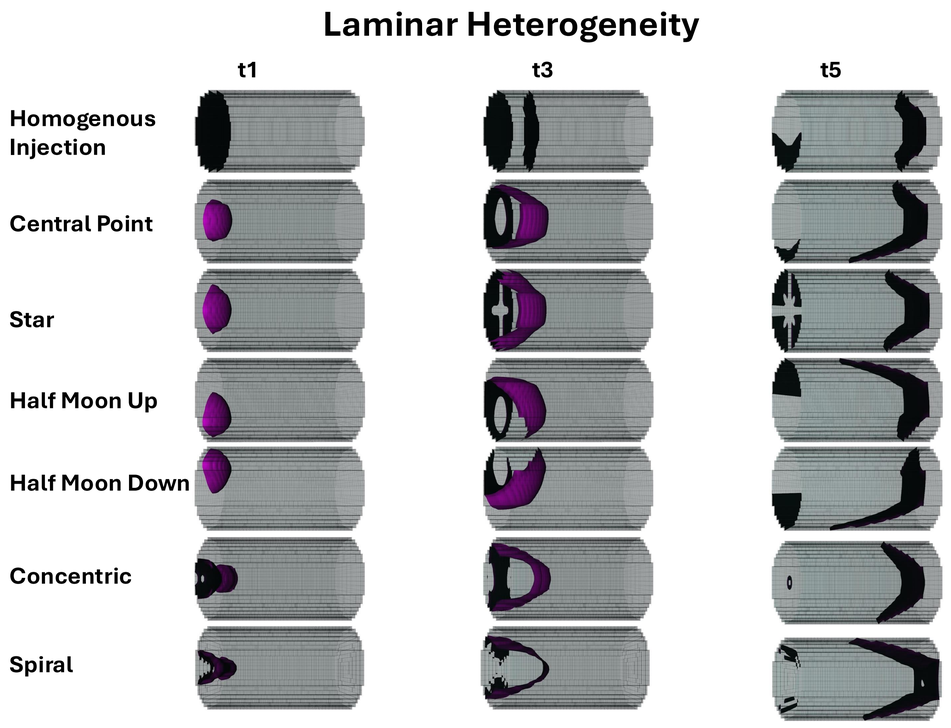

Fig. 3: Water saturation frontal advance with Sw = 0.21 for laminar scenario.

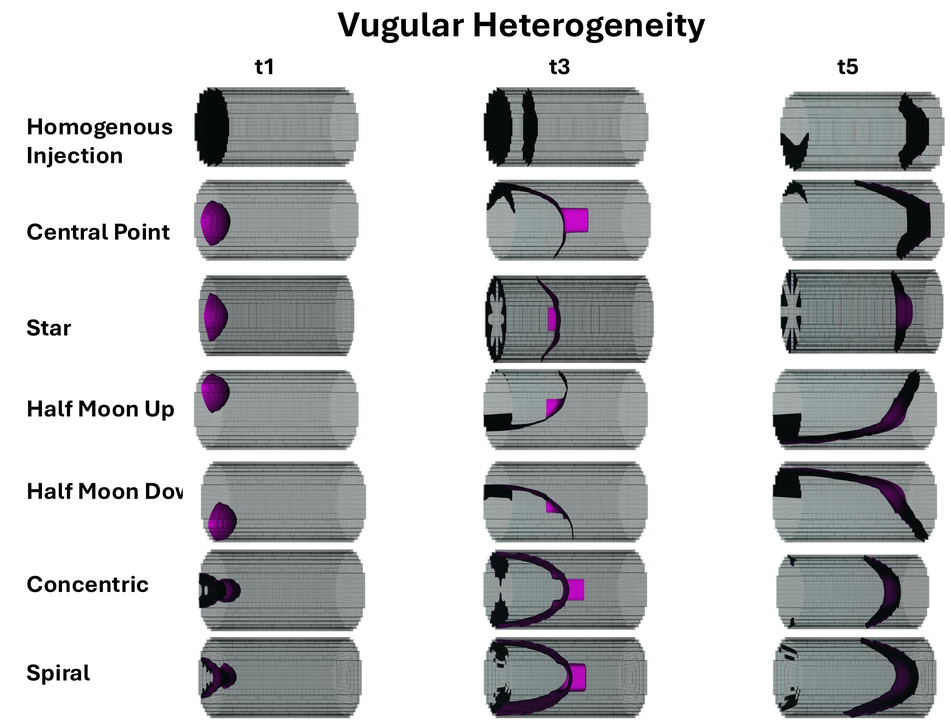

Fig. 4: Water saturation frontal advance with Sw = 0.21 for vugular scenario.

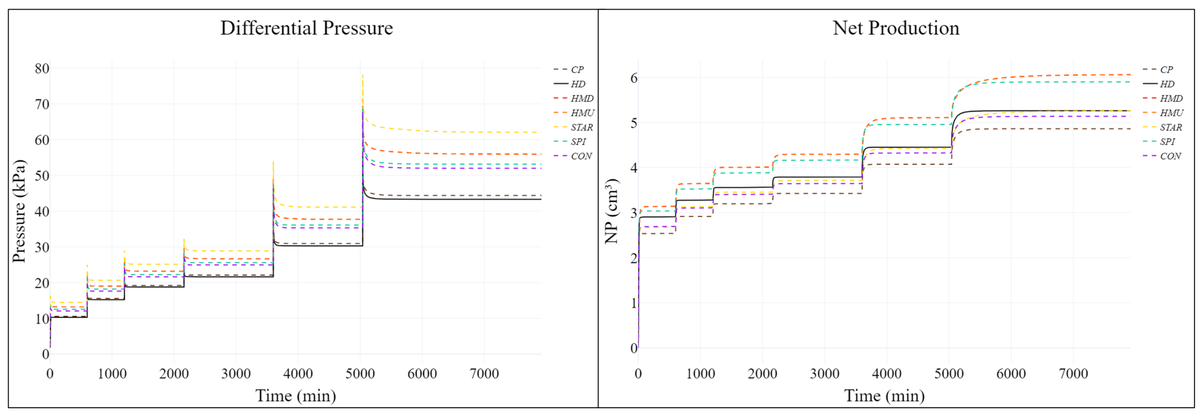

Fig. 5: Differential Pressure and Net Production curves.

Conclusions

- Inlet diffuser geometry strongly affects flow behavior, even with uniform saturation fronts, due to gravity-induced symmetry breaking;
- Simulations in homogeneous, laminated, and vuggy media confirm the significant influence of diffuser design;
- Prior knowledge of the experimental diffuser is essential for reliable uncertainty quantification;
- Accounting for diffuser geometry prevents misinterpretation and improves sensitivity and calibration study design.

This research was carried out in association with the ongoing R&D project registered as ANP nº 24.551, “Avaliação de Metodologias para Interpretação de Curvas de Permeabilidade Relativa em meios porosos heterogêneos" (UFRJ/Petrobras Brasil/ANP), sponsored by Petróleo Brasileiro S/A under the ANP R&D levy as “Compromisso de Investimentos com Pesquisa e Desenvolvimento”.

Rien van Genuchten Conference

DEVELOPING A SIMPLIFIED LANDSLIDE ALERT MODEL FOR PETRÓPOLIS, BRAZIL, USING HYDRUS 1D

Cristiane Ribeiro de Melo [1]; Marta Vasconcelos Ottoni [2] & Paulo Abadie Guedes [3]

1) Serviço Geológico do Brasil. Rua Escritor Souza Barros, 1001 - Cabanga Recife, PE, Brasil. e-mail: cristiane.melo@sgb.gov.br
2) Serviço Geológico do Brasil. Av. Pasteur, 404 – Urca, Rio de Janeiro, RJ, Brasil. e-mail: marta.ottoni@sgb.gov.br
3) Instituto Federal de Pernambuco. Av. Prof. Luís Freire, 500 - CDU, Recife, PE, Brasil. e-mail: paulo.guedes@recife.ifpe.edu.br

INTRODUCTION

The increase in soil pore pressure due to rainfall infiltration is a triggering factor for landslides. Some countries use soil water balance models in their Landslide Early Warning Systems (LEWSs) to identify the soil saturation level and the precipitation threshold, capable of triggering such events. In Brazil, in the Quitandinha neighborhood, in Petrópolis/RJ, there is a high frequency of landslides. This work proposes a simplified model for regional landslide alerts, evaluating the linearity trend between accumulated simulated infiltration and accumulated precipitation in locations close to landslide areas, from September to December 2021.

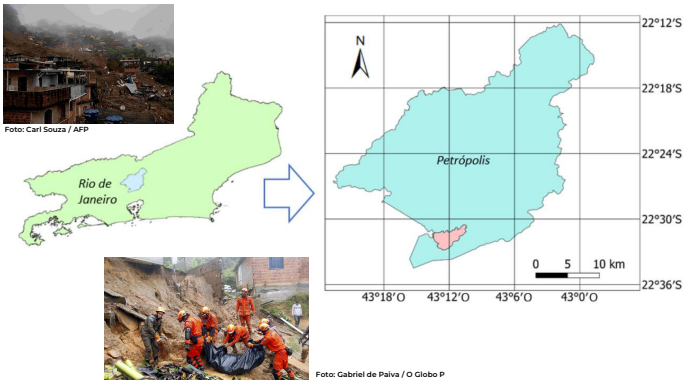

Figure 1. Location of the Quitandinha river basin (Source: Gonzalez *et al.*, 2021)

METHODOLOGY

Infiltrations were simulated using HYDRUS-1D (PC-progress, 2025) in two locations: a forest area and an urbanized area, both close to a landslide location. The event of 12/18/2021, recorded by civil defense and the media, served as a reference for the simulation, which started in September (dry month) and extended for three consecutive rainy months. Precipitation data from the Rua Amazonas station (code 2243433), from the National Center for Monitoring and Alerts for Natural Disasters - CEMADEN, were used, and soil parameters were obtained through field and laboratory tests, including saturated hydraulic conductivity (K_{sat}) at three depths, up to 1.70m. Result validation was performed with volumetric moisture data from the EnviroSCAN probe (CEMADEN, 2024). The linear trend between accumulated precipitation and accumulated infiltration was evaluated together with information from other landslides that occurred in the area.

RESULTS

The results revealed a linear trend between accumulated simulated infiltration and accumulated precipitation, up to the landslide date, in the two locations analyzed (Figure 6). The research continues, evaluating whether this linearity is repeated in other points of the water basin, enabling the creation of a simple model to estimate landslide probability, based only on infiltration and precipitation data.

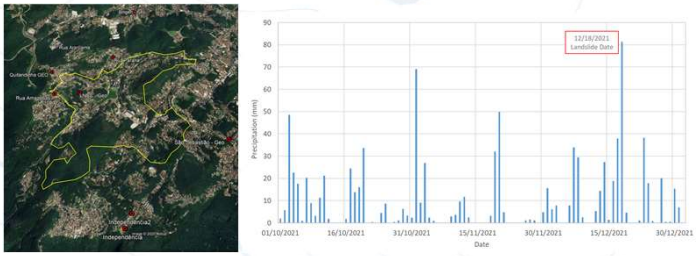

Figure 2. Spatialization of the rainfall network and rainfall series

Table 1. Sample collection points

Address	Date	Susceptibility Class	1° depth (m)	2° depth (m)	3° depth (m)
Rua Minas Gerais	17/07/2024	High	0.50 – 1.05	1.15 – 1.68	
Rua Paraná	18/07/2024	Low / Medium	0.50 – 0.90	1.10 – 1.50	1.50 – 1.70

Figure 3. Sample collection points (in yellow) and landslides registered by Civil Defense (in red)

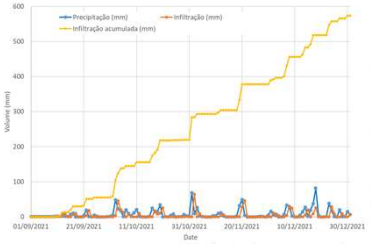

Figure 4. Soil water balance

Figure 5. Validation of simulated infiltration

The soil types found at different depths were sandy clay loam and sandy loam. The soil water balance for the event on 12/18/2021 showed a similar infiltrated total for the two soil sampling points.

Table 2. Accumulated precipitation and infiltration for landslide events

Event	Precipitation on the day (mm)	Accumulated			% infiltrated in relation to precipitation
		Precipitation (mm)	Infiltration (mm)	Runoff (mm)	
10/11/2021	21.20	237.00	156.05	80.95	65.8
10/20/2021	33.7	328.60	218.00	110.60	66.3
11/01/2021	69.1	425.20	284.20	141.00	66.8
11/03/2021	27.0	461.30	293.57	167.73	63.6
12/18/2021	81.3	884.5	518.04	366.46	58.6

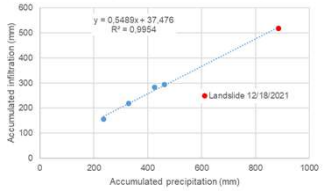

Figure 6. Trend between the event that occurred on 12/18/2021 and other landslides in the studied region

CONCLUSIONS

Our preliminary findings suggest a promising linear relationship between accumulated rainfall and simulated soil infiltration as a potential indicator for landslide occurrence in Petrópolis. This simplified approach offers a potential pathway for developing a regional landslide early warning system. Further research is crucial to validate this linear trend across a wider area and to determine its reliability and lead time for accurate predictions. Ultimately, this work contributes to a practical understanding of infiltration's role in triggering landslides and offers a basis for future, more comprehensive early warning strategies.

REFERENCES

GONZALEZ, F. C. G.; MENDONÇA, M. B. & COELHO, Gl. V. S. (2021). In: Anais: VIII Conferência Brasileira sobre Estabilidade de Encostas. Porto de Galinhas, PE. PC-progress. Engineering Software Developer. HYDRUS-1D. (2025). Disponível em: https://www.pc-progress.com/en/Default.aspx?hydrus-1d em abril de 2025.

SGB SERVIÇO GEOLÓGICO DO BRASIL
MINISTÉRIO DE MINAS E ENERGIA
GOVERNO FEDERAL BRASIL UNIÃO E RECONSTRUÇÃO

Modelling the effects of compaction on soil water retention and infiltration

Duc Ngo-Cong [1], Diogenes L. Antille [2,*], Martinus Th. van Genuchten [3,4], Rafael D. L'Abbate [5], Reginaldo Barboza da Silva [5]

[1] Formerly at University of Southern Queensland, Centre for Agricultural Engineering, Toowoomba QLD, Australia; [2] CSIRO Agriculture and Food, Canberra ACT, Australia; [3] Utrecht University, Department of Earth Sciences, The Netherlands; [4] Universidade Federal do Rio de Janeiro, Departamento de Engenharia Nuclear, Rio de Janeiro, Brazil; [5] Universidade Estadual Paulista, Faculdade de Ciências Agrárias, Registro SP, Brazil. Correspondence: * Dio.Antille@csiro.au

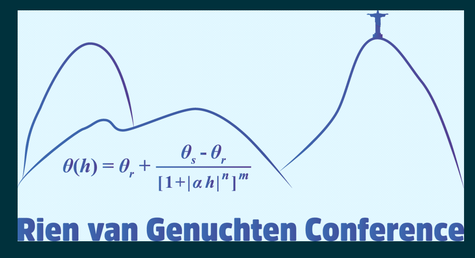

Challenges and Opportunities in Porous Media Multiphase Flow and Contaminant Transport Research
Universidade Federal do Rio de Janeiro, Brazil, 7th – 9th May 2025

CSIRO SOIL PROCESS AND FUNCTION TEAM
www.csiro.au

BACKGROUND

- Soil compaction (increased soil bulk density) has detrimental effects on the physical and hydraulic properties of soils, thereby affecting important plant-soil-water processes that influence crop productivity.
- Key soil properties affected by compaction are soil water retention and water infiltration into soil because of the changes in pore size and size distribution, and disruption on pores' connectivity. Numerical approaches can be used with confidence to quantify such effects; thus, reducing the need for field and laboratory measurements.

OBJECTIVES

- To develop numerical approaches for determining the effects of soil compaction on the water retention curve (WRC), and
- To quantify the effects of soil compaction on the plant available water capacity (PAWC) and infiltration characteristics of a wide range of soils from the US and Australia.

MATERIALS AND METHODS

- A total of 14 different soil series, spanning geographic distributions across the US (7 soil series) and Australia (7 soil series), were used for the analysis.
- The van Genuchten-Mualem (VG) model was used to describe the soil water retention and hydraulic conductivity functions. The VG parameters θ_{sc} and θ_{rc} of compacted soil were determined as a function of the non-compacted parameters (θ_s, θ_r and ρ_b) and the soil bulk density of compacted soil (ρ_{bc}).
- The VG parameters α and exponent η after compaction were estimated using two approaches. Approach 1: α and η were determined by fitting the data of the saturation, 15 bar and residual water contents. Approach 2: η was assumed to remain unchanged with compaction because the CV for η was small compared with the CV values of all other hydraulic parameters (θ_s, θ_r, α, and K_s), consistent with Carsel and Parrish (1988) and Approach 1's results. Hence, the parameter α could be determined from the VG equation.
- The WRCs modelled for different design ρ_b (assuming increments of 10%, 20% and 30% in the compaction level) were combined with the HYDRUS-1D model to simulate vertical water infiltration into both non-compacted and compacted soils.

Table 1. Model validation: Root-Mean-Square Error (RMSE) and R^2 values between measured and modelled soil WRCs for US* and Australian** soils at the design soil bulk densities (ρ_{bc}). SD: Standard deviation (for mean values across all soil series and soil bulk densities).

Soil series	Modeling approach	Approach 1		Approach 2		Soil texture
Parameter	Measured ρ_b (g cm^{-3})	RMSE (m^3 m^{-3})	R^2 (-)	RMSE (m^3 m^{-3})	R^2 (-)	(clay content, % w/w)
Mountview*	1.11	0.042	0.86	0.042	0.86	Silt loam (16.3%)
	1.24	0.041	0.89	0.035	0.92	
	1.45	0.061	0.73	0.070	0.65	
Lexington*	1.43	0.017	0.99	0.017	0.99	Silt loam (13.6%)
	1.51	0.020	0.97	0.017	0.98	
Grenada*	1.14	0.020	0.97	0.020	0.97	Fine silt (14.3%)
	1.32	0.045	0.90	0.039	0.93	
Dewey*	1.39	0.016	0.94	0.016	0.94	Silty clay loam (30.6%)
	1.52	0.039	0.70	0.029	0.84	
Columbia*	1.22	0.010	1.00	0.010	1.00	Sandy loam (11%)
	1.28	0.029	0.96	0.022	0.98	
	1.34	0.051	0.86	0.040	0.92	
Coto*	1.06	0.006	1.00	0.006	1.00	Clay (60.5%)
	1.22	0.019	0.84	0.019	0.84	
Griffith**	1.00	0.028	0.93	0.028	0.93	Clay (44%)
	1.30	0.071	0.69	0.070	0.70	
Gunber**	1.03	0.028	0.91	0.028	0.91	Clay (47%)
	1.21	0.067	0.34	0.047	0.68	
Average	-	0.034	0.86	0.031	0.89	-
SD	-	± 0.0197	± 0.162	± 0.0183	± 0.111	-

RESULTS

- Approach 2 provided a better agreement with measured data than Approach 1, but both approaches yielded satisfactory solutions and can be used with confidence (Table 1).
- Since Approach 2 performed slightly better than Approach 1, the analysis only considered the application of Approach 2. The effects of compaction on the VG-WRC parameters, infiltration characteristics and PAWC are shown in Figures 1-3, respectively.

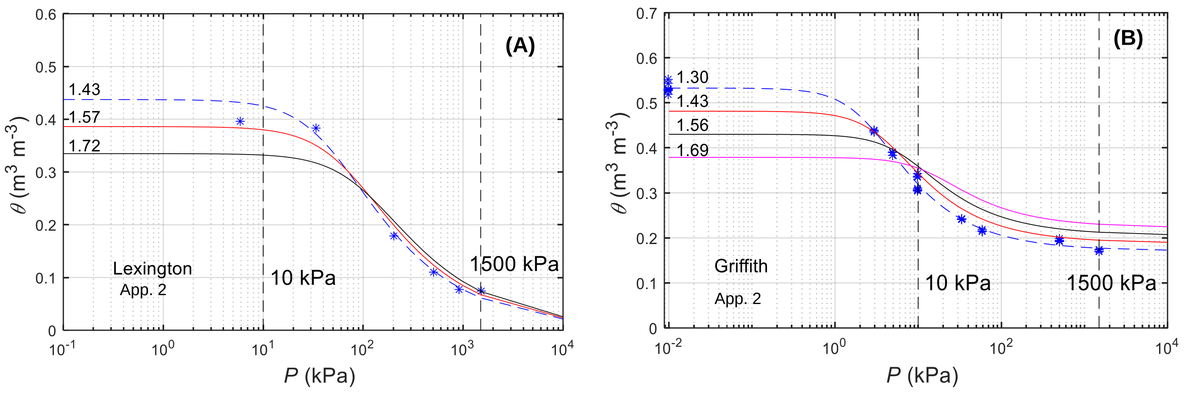

Figure 1. In (A): WRC of Lexington series without compaction (ρ_b =1.43 g cm^{-3}) and at two different levels of compaction (ρ_b =1.57 and 1.72 g cm^{-3}, respectively), and (B): Griffith series without compaction (ρ_b =1.30 g cm^{-3}) and at three different levels of compaction (ρ_b = 1.43, 156 and 1.69 g cm^{-3}, respectively).

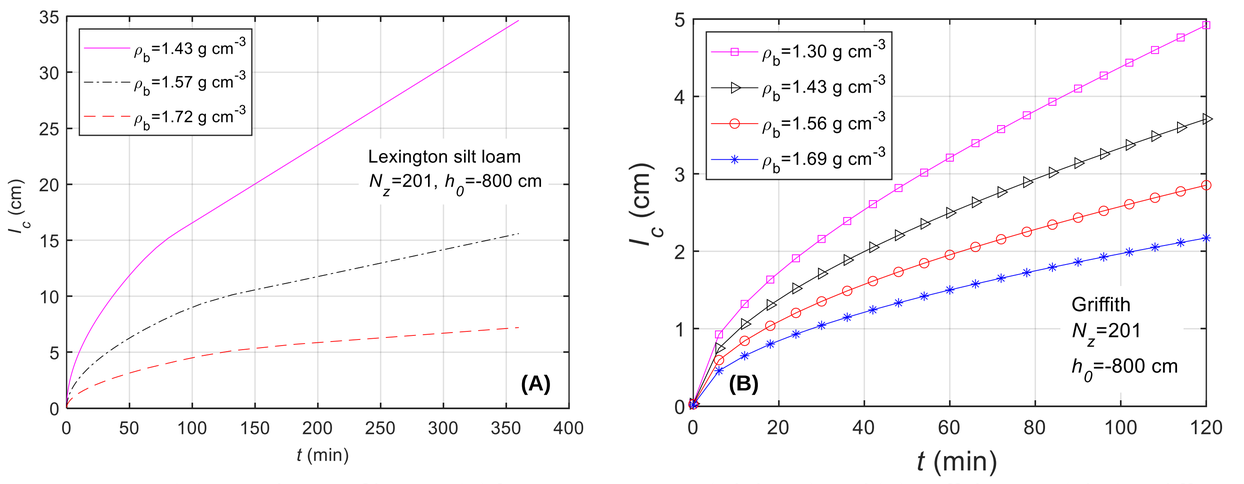

Figure 2. In (A): cumulative infiltration (I_c) for Lexington series (Silt loam), and (B) Griffith series (Clay) at different soil bulk densities.

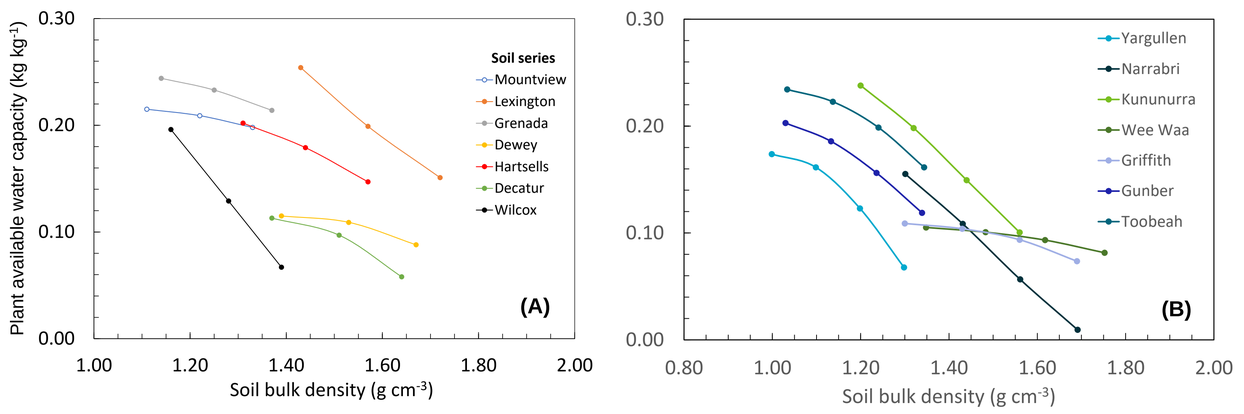

Figure 3. The effect of soil bulk density on plant available water capacity for a range of soil types. In (A): USA soils (clay content: ~10 to 60% w/w), and (B): Australian soils (clay content: ~45 to 75% w/w).

CONCLUSIONS AND FURTHER WORK

- The two numerical approaches developed during this study expanded the applicability of the VG model to quantify the effect of soil compaction on the WRC. There was good agreement between measured and modelled data.
- Key results showed that a 10-30% increase in soil bulk density (due to compaction) reduced cumulative infiltration at $T=T_{final}$ (steady-state) by ~25-94% and PAWC by ~3-94%, depending upon soil type and textural class.
- The proposed modelling framework can be used with confidence for a wide range of soil types to study the hydrology of compacted soils.
- Adoption of mechanization systems that mitigate (e.g., low-ground tyre pressure) or avoid (e.g., controlled traffic farming) soil damage due to compaction is a pre-requisite for improving soil water retention and water-use efficiency by crops.

FUNDING AND ACKNOWLEDGEMENTS

This research received financial and operational support from Cotton Incorporated (Cary NC, USA; https://www.cottoninc.com/), the Centre for Agricultural Engineering at the University of Southern Queensland (Toowoomba, QLD, Australia), and CSIRO Agriculture and Food (Australia).

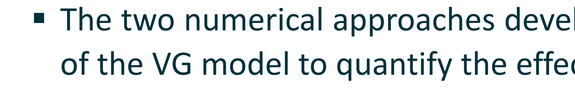
Received: 2 March 2021 | Accepted: 25 August 2021 | Published online: 27 October 2021
DOI: 10.1002/saj2.20328
SOIL PHYSICS & HYDROLOGY
Soil Science Society of America Journal
A modeling framework to quantify the effects of compaction on soil water retention and infiltration
Duc Ngo-Cong[1] | Diogenes L. Antille[1,2] | Martinus Th. van Genuchten[3,4] | Hung Q. Nguyen[1] | Mehari Z. Tekeste[5] | Craig P. Baillie[1] | Richard J. Godwin[6]

REFERENCES

- Carsel, R.F., Parrish, R.S. (1988). *Water Resources Research, 24*(5): 755-769. https://doi.org/10.1029/WR024i005p00755.
- Ngo-Cong, D., Antille, D.L., van Genuchten, M.Th., *et al.* (2021): *Soil Science Society of America, 85*(6): 1931-1945. https://doi.org/10.1002/saj2.20328.

Open-access inventory of pedotransfer functions for hydraulic properties in Brazilian soils

Authors: Bruna Vicente Sturm[1], Marta Vasconselos Ottoni[2], Quirijn de Jong van Lier, Nilton Curi, José Miguel Reichert

Rien van Genuchten Conference

Introduction

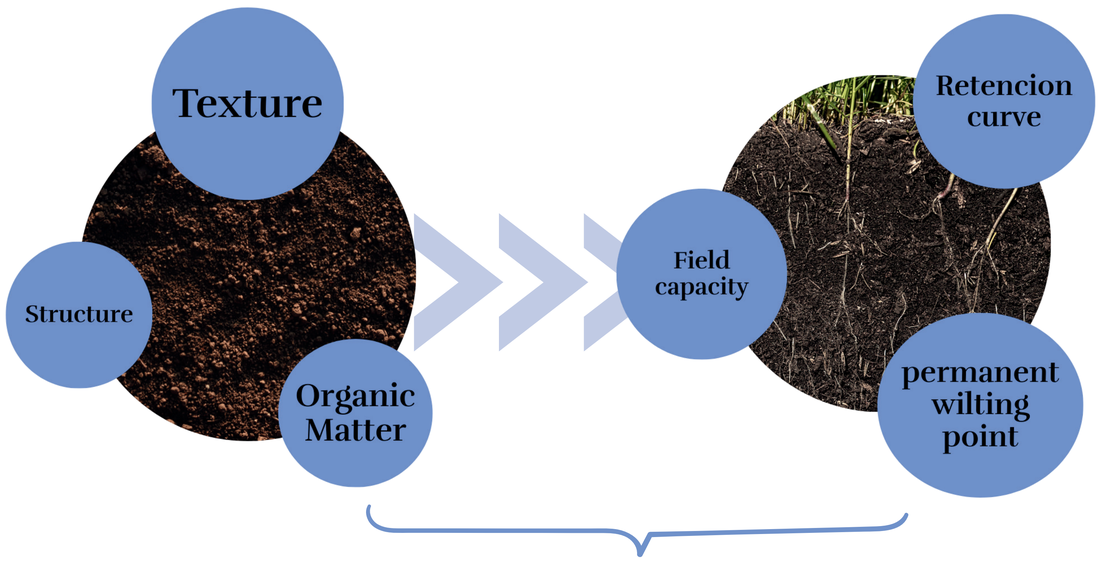

PTFs are dispersed, complicating access and leading to recalibrations that are often redundant.

Objectives

Create an open-access inventory of Brazilian PTFs for hydraulic properties and provide recommendations for their widespread application

Methodology

This study compiled 468 Brazilian PTFs from scientific literature between 1987 and 2023. The models were classified into two categories:

1. Point-based PTFs (309 models): estimate water content at field capacity and wilting point.
2. Parameter-based PTFs (159 models): predict van Genuchten retention parameters.

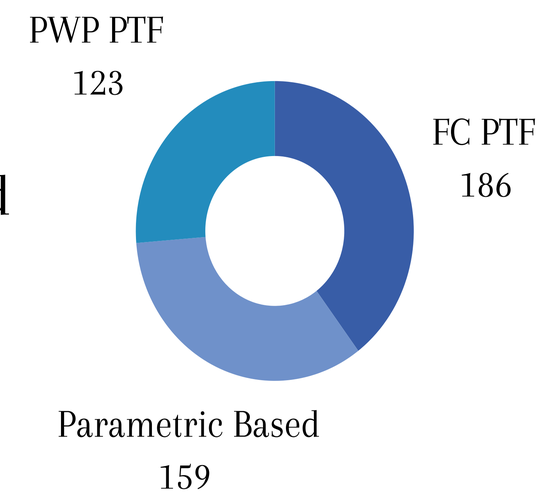

A statistical analysis was performed of these models to identify trends in development, predictors used, and methodologies applied.

Results

Point based PTF

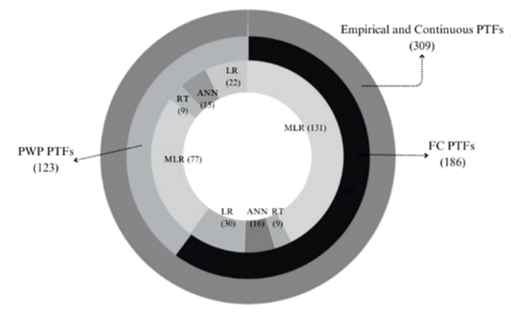

Parameter based PTF

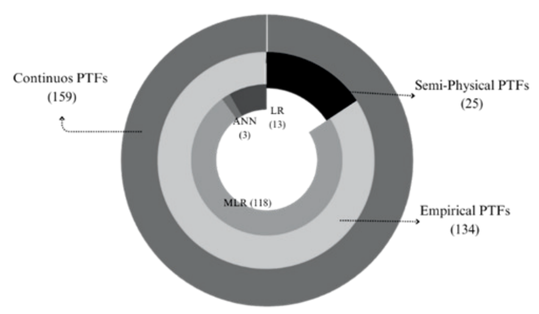

Multiple linear regression was the most common approach in point-based PTFs and parameter-based PTFs increasingly rely on machine learning, especially artificial neural networks.

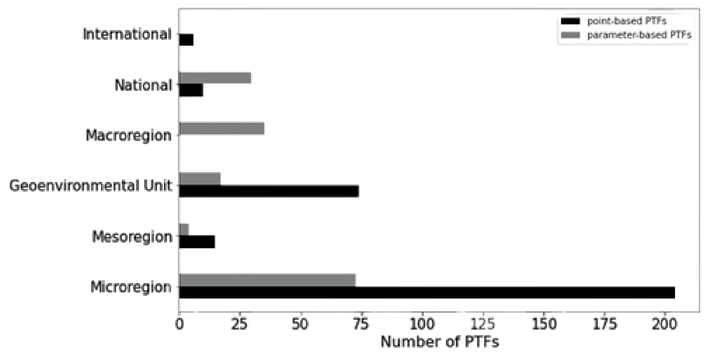

Most models were developed at the state level, with few covering the national scale

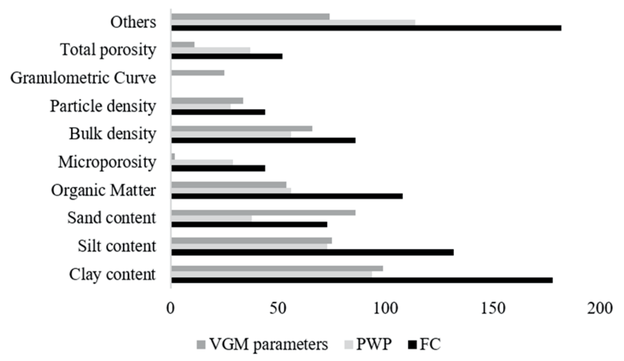

Soil physical properties particularly particle size distribution, were the most used predictors.

Conclusion

There is an urgent need for nationally applicable PTFs to enhance soil modeling in Brazil.

We recommend:

- Standardizing the reporting of calibration and validation errors.
- Improving transparency in model development.
- Increasing accessibility through open repositories.

[1]bruna.vicente@acad.ufsm.br
[2]marta.ottoni@sgb.gov.br

CPRM Serviço Geológico do Brasil

Programa de Pós-Graduação em Ciência do Solo - UFSM

Universidade Federal de Santa Maria 1960

A systematic global recharacterization method for reservoir fluids in compositional simulations

Barbara F. Esteves[(a)], Fellipe C. de Oliveira[(a)], Paulo Couto[(b)], and Paulo L.C. Lage[(a)]

(a) Department of Chemical Engineering, COPPE/UFRJ (b) Department of Civil Engineering, COPPE/UFRJ

INTRODUCTION

Compositional reservoir simulations + Complex fluid compositions → High computational costs! → Mitigation strategy

Lumping schemes are employed to pseudoize the fluid description, substituting its originally identified components by a reduced number of pseudo-components.

Lumping strategies for the C_{7+} fraction are readily available. However, standard global schemes are still missing in the literature.

Objective

This study aims to present an accurate and systematic global recharacterization strategy.

METHODOLOGY

Global recharacterization strategy

Discrete components

1) Carbon dioxide (CO_2) remains ungrouped.
2) Methane (CH_4) groups only with nitrogen (N_2).
3) Ethane (C_2H_6) and propane (C_3H_8) remain ungrouped
4) Components with four and five carbon atoms form a single group when applying the method of Lage to the C_{6+} fraction. Similarly, components with four, five, and six carbons form a single group when recharacterizing the C_{7+} fraction.

C_+ fraction components

The adaptive method of Lage calculates the Gauss-Christofell quadrature rule from the moments of the molar fraction discrete distribution in terms of the molar mass to recharacterize the plus fraction described by SCN components (see QR code for the public repository where the code is freely available).

Reservoir model

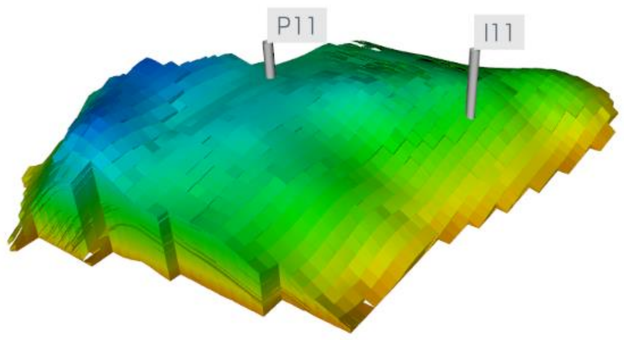

- A modified version of model UNISIM-IV-2019 for subsurface reservoirs was used.
- Porosity and permeability considered, respectively, a normal distribution and a log-normal distribution.
- A maximum surface gas rate for the injector well and a maximum total surface liquid rate constraint for the producer well are considered.
- This study employed the commercial compositional reservoir simulator CMG GEM.

Fluids

- The **original** reservoir fluid composition used in this study is described in the table below.
- **Alavian's** characterization is our benchmark composition obtained by optimization techniques and the use of weighting factors.
- **R1** and **R2** are rechracterized compositions obtained by the strategy proposed here.

Characterization	Components
Original	N_2, CO_2, CH_4, C_2H_6, C_3H_8, iC_4, nC_4, iC_5, nC_5, C_6, C_7, C_8, C_9, C_{10}, C_{11}, C_{12}, C_{13}, C_{14}, C_{15}, C_{16}, C_{17}, C_{18}, C_{19}, C_{20}, C_{21}, C_{22}, C_{23}, C_{24}, C_{25}, C_{26}, C_{27}, C_{28}, C_{29}, C_{30+}
Alavian's	N_2, CO_2, CH_4, C_2 - C_3, C_4 - C_6, C_7 -C_{11}, C_{12} - C_{15}, C_{16} - C_{23}, C_{24} - C_{30+}
R1	CO_2, N_2 - CH_4, C_2 , C_3, C_4 - C_6, and 4 pseudos for C_{7+}
R2	CO_2, N_2 - CH_4, C_2 , C_3, C_4 - C_5, and 4 pseudos for C_{6+}

RESULTS AND DISCUSSION

Phase diagram

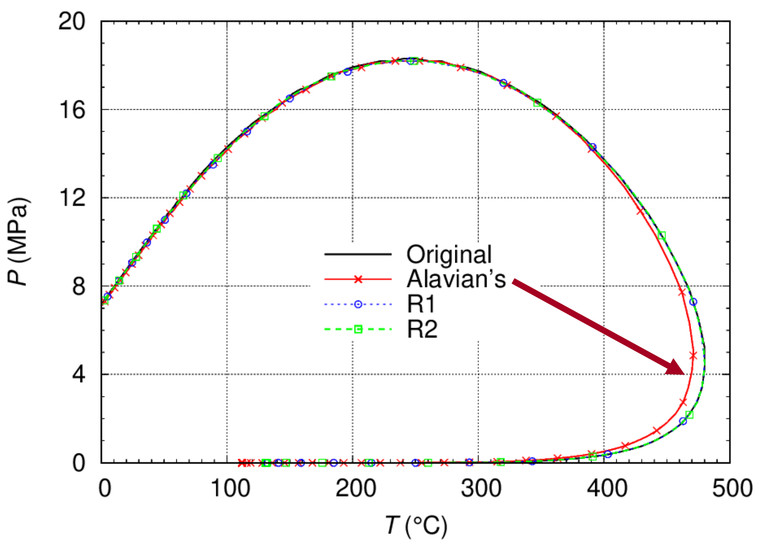

- Phase diagrams for the reservoir mixture using the original composition and recharacterizations given by our method and that proposed by the benchmark study.
- **R1** and **R2** compositions presented **better representations** of the original curve compared to Alavian's, particularly for T > 400 °C (see red curve).
- Note that Alavian's method needs to test **142.506 lumping combinations** and assumed **tunned parameters** to reach its best-case scenario.

Reservoir simulations

Global mole fraction of CO_2

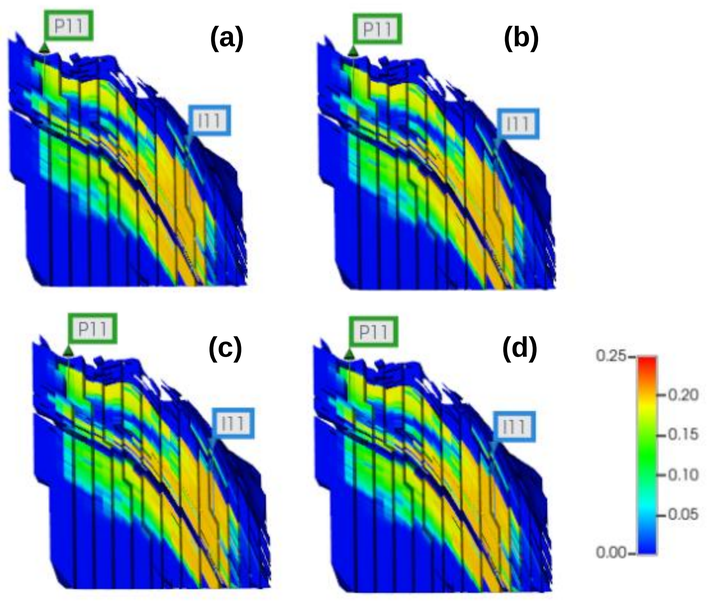

- Global mole fraction of CO_2 of the reservoir mixture in a reservoir section view after breakthrough: **(a)** Original composition, **(b)** Alavian's, **(c)** R1, and **(d)** R2.
- All recharacterizations represented well the original composition. However, it is important to remember that the **benchmark strategy is more costly and less systematic**.
- Note that **recharacterized composition** simulations presented run-times approximately **7× faster** than the original one.

Gas-oil ratio

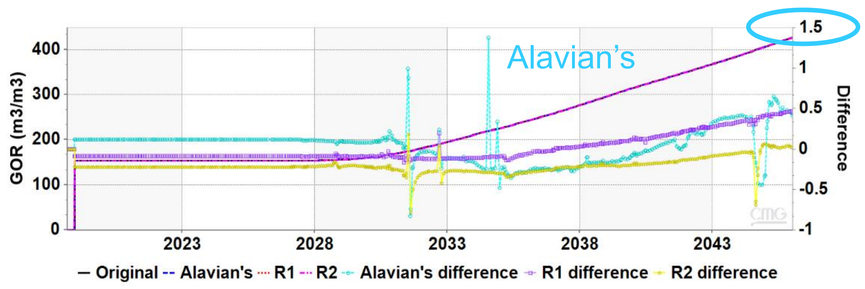

Hydrocarbon recovery factor

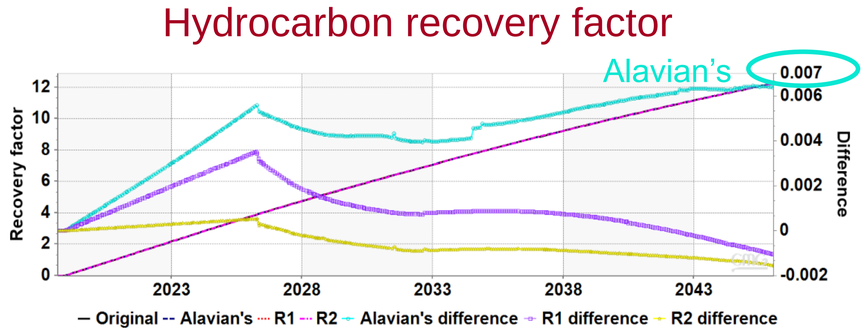

- GOR and recovery factor performance for original and recharacterized compositions were similar.
- The **secondary axis** shows the **absolute difference** between properties from the recharacterized and original compositions.
- Alavian's recharacterization always presented the largest differences.

ACKNOWLEDGEMENTS

This research was carried out in association with the ongoing R&D project registered as ANP nº 23209-0, "Caracterização de Fluidos Complexos em Condições de Reservatórios: Avaliação do Comportamento de Fases de Fluidos de Reservatórios Sob a Presença de CO_2" (UFRJ/Shell Brasil/ANP), sponsored by Shell Brasil Petróleo Ltda under the ANP R&D levy as "Compromisso de Investimentos com Pesquisa e Desenvolvimento". This study was financed in part by the Coordenação de Aperfeiçoamento de Pessoal de Nível Superior – Brasil (CAPES) – Finance Code 001. Paulo L.C. Lage and Paulo Couto acknowledge the financial support from CNPq through processes 303845/2022-8 and 311143/2022-9, respectively.

REFERENCES

The full discussion of this study can be found in our publication in the ***Geoenergy Science and Engineering journal*** (see the QR code for more details).

Modelling the effects of compaction on soil water retention and infiltration

Duc Ngo-Cong [1], Diogenes L. Antille [2,*], Martinus Th. van Genuchten [3,4]

[1] Formerly at University of Southern Queensland, Centre for Agricultural Engineering, Toowoomba QLD, Australia; [2] CSIRO Agriculture and Food, Canberra ACT, Australia; [3] Utrecht University, Department of Earth Sciences, The Netherlands; [4] Universidade Federal do Rio de Janeiro, Departamento de Engenharia Nuclear, Rio de Janeiro, Brazil. Correspondence: * Dio.Antille@csiro.au

Rien van Genuchten Conference

Challenges and Opportunities in Porous Media Multiphase Flow and Contaminant Transport Research
Universidade Federal do Rio de Janeiro, Brazil, 7th – 9th May 2025

CSIRO SOIL PROCESS AND FUNCTION TEAM
www.csiro.au

BACKGROUND

- Soil compaction (increased soil bulk density) has detrimental effects on the physical and hydraulic properties of soils, thereby affecting important plant-soil-water processes that influence crop productivity.
- Key soil properties affected by compaction are soil water retention and water infiltration into soil because of the changes in pore size and size distribution, and disruption on pores' connectivity. Numerical approaches can be used with confidence to quantify such effects; thus, reducing the need for field and laboratory measurements.

OBJECTIVES

- To develop numerical approaches for determining the effects of soil compaction on the water retention curve (WRC), and
- To quantify the effects of soil compaction on the plant available water capacity (PAWC) and infiltration characteristics of a wide range of soils from the US and Australia.

MATERIALS AND METHODS

- A total of 14 different soil series, spanning geographic distributions across the US (7 soil series) and Australia (7 soil series), were used for the analysis.
- The van Genuchten-Mualem (VG) model was used to describe the soil water retention and hydraulic conductivity functions. The VG parameters θ_{sc} and θ_{rc} of compacted soil were determined as a function of the non-compacted parameters (θ_s, θ_r and ρ_b) and the soil bulk density of compacted soil (ρ_{bc}).
- The VG parameters α and exponent η after compaction were estimated using two approaches. Approach 1: α and η were determined by fitting the data of the saturation, 15 bar and residual water contents. Approach 2: η was assumed to remain unchanged with compaction because the CV for η was small compared with the CV values of all other hydraulic parameters (θ_s, θ_r, α, and K_s), consistent with Carsel and Parrish (1988) and Approach 1's results. Hence, the parameter α could be determined from the VG equation.
- The WRCs modelled for different design ρ_b (assuming increments of 10%, 20% and 30% in the compaction level) were combined with the HYDRUS-1D model to simulate vertical water infiltration into both non-compacted and compacted soils.

Table 1. Model validation: Root-Mean-Square Error (RMSE) and R^2 values between measured and modelled soil WRCs for US* and Australian** soils at the design soil bulk densities (ρ_{bc}). SD: Standard deviation (for mean values across all soil series and soil bulk densities).

Soil series	Modeling approach	Approach 1		Approach 2		Soil texture
Parameter	Measured ρ_b (g cm^{-3})	RMSE (m^3 m^{-3})	R^2 (-)	RMSE (m^3 m^{-3})	R^2 (-)	(clay content, % w/w)
Mountview*	1.11	0.042	0.86	0.042	0.86	Silt loam (16.3%)
	1.24	0.041	0.89	0.035	0.92	
	1.45	0.061	0.73	0.070	0.65	
Lexington*	1.43	0.017	0.99	0.017	0.99	Silt loam (13.6%)
	1.51	0.020	0.97	0.017	0.98	
Grenada*	1.14	0.020	0.97	0.020	0.97	Fine silt (14.3%)
	1.32	0.045	0.90	0.039	0.93	
Dewey*	1.39	0.016	0.94	0.016	0.94	Silty clay loam (30.6%)
	1.52	0.039	0.70	0.029	0.84	
Columbia*	1.22	0.010	1.00	0.010	1.00	Sandy loam (11%)
	1.28	0.029	0.96	0.022	0.98	
	1.34	0.051	0.86	0.040	0.92	
Coto*	1.06	0.006	1.00	0.006	1.00	Clay (60.5%)
	1.22	0.019	0.84	0.019	0.84	
Griffith**	1.00	0.028	0.93	0.028	0.93	Clay (44%)
	1.30	0.071	0.69	0.070	0.70	
Gunber**	1.03	0.028	0.91	0.028	0.91	Clay (47%)
	1.21	0.067	0.34	0.047	0.68	
Average	-	0.034	0.86	0.031	0.89	-
SD	-	± 0.0197	± 0.162	± 0.0183	± 0.111	-

RESULTS

- Approach 2 provided a better agreement with measured data than Approach 1, but both approaches yielded satisfactory solutions and can be used with confidence (Table 1).
- Since Approach 2 performed slightly better than Approach 1, the analysis only considered the application of Approach 2. The effects of compaction on the VG-WRC parameters, infiltration characteristics and PAWC are shown in Figures 1-3, respectively.

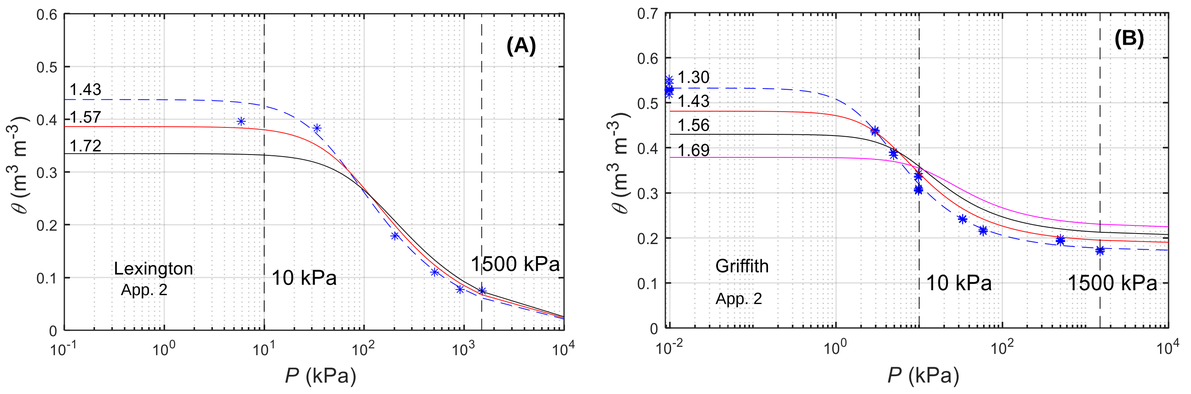

Figure 1. In (A): WRC of Lexington series without compaction (ρ_b =1.43 g cm^{-3}) and at two different levels of compaction (ρ_b =1.57 and 1.72 g cm^{-3}, respectively), and (B): Griffith series without compaction (ρ_b =1.30 g cm^{-3}) and at three different levels of compaction (ρ_b = 1.43, 156 and 1.69 g cm^{-3}, respectively).

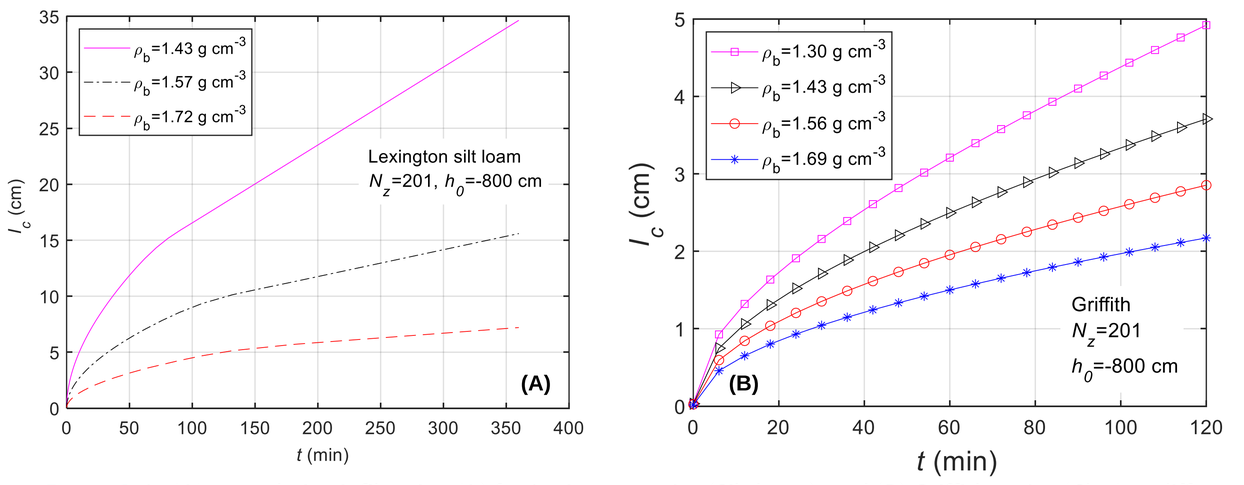

Figure 2. In (A): cumulative infiltration (I_c) for Lexington series (Silt loam), and (B) Griffith series (Clay) at different soil bulk densities.

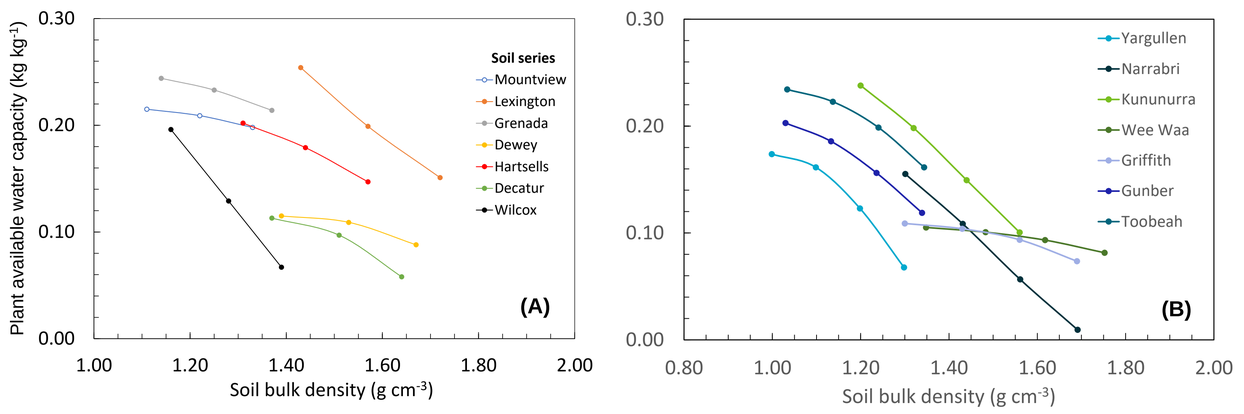

Figure 3. The effect of soil bulk density on plant available water capacity for a range of soil types. In (A): USA soils (clay content: ~10 to 60% w/w), and (B): Australian soils (clay content: ~45 to 75% w/w).

CONCLUSIONS AND FURTHER WORK

- The two numerical approaches developed during this study expanded the applicability of the VG model to quantify the effect of soil compaction on the WRC. There was good agreement between measured and modelled data.
- Key results showed that a 10-30% increase in soil bulk density (due to compaction) reduced cumulative infiltration at $T=T_{final}$ (steady-state) by ~25-94% and PAWC by ~3-94%, depending upon soil type and textural class.
- The proposed modelling framework can be used with confidence for a wide range of soil types to study the hydrology of compacted soils.
- Adoption of mechanization systems that mitigate (e.g., low-ground tyre pressure) or avoid (e.g., controlled traffic farming) soil damage due to compaction is a pre-requisite for improving soil water retention and water-use efficiency by crops.

FUNDING AND ACKNOWLEDGEMENTS

This research received financial and operational support from Cotton Incorporated (Cary NC, USA; https://www.cottoninc.com/), the Centre for Agricultural Engineering at the University of Southern Queensland (Toowoomba, QLD, Australia), and CSIRO Agriculture and Food (Australia).

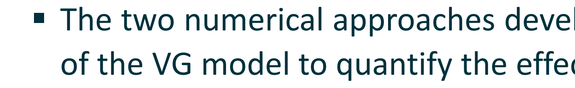
Received: 2 March 2021 | Accepted: 25 August 2021 | Published online: 27 October 2021
DOI: 10.1002/saj2.20328
SOIL PHYSICS & HYDROLOGY
Soil Science Society of America Journal
A modeling framework to quantify the effects of compaction on soil water retention and infiltration
Duc Ngo-Cong[1] | Diogenes L. Antille[1,2] | Martinus Th. van Genuchten[3,4] | Hung Q. Nguyen[1] | Mehari Z. Tekeste[5] | Craig P. Baillie[1] | Richard J. Godwin[6]

REFERENCES

- Carsel, R.F., Parrish, R.S. (1988). *Water Resources Research, 24*(5): 755-769. https://doi.org/10.1029/WR024i005p00755.
- Ngo-Cong, D., Antille, D.L., van Genuchten, M.Th., *et al.* (2021): *Soil Science Society of America, 85*(6): 1931-1945. https://doi.org/10.1002/saj2.20328.

A NOVEL APPLICATION OF HYDRUS-1D: MODELING OVERLAND SOLUTE TRANSPORT DURING FURROW FERTIGATION

Ali Ashrafi[1], Martinus Th. van Genuchten[2,3], Behzad Ghanbarian[4,5,6], Hamed Ebrahimian[7*]

[1]Department of Plant and Soil Sciences, Oklahoma State University, Stillwater, OK, USA.
[2]Department of Nuclear Engineering, Federal University of Rio de Janeiro, Rio de Janeiro, Brazil.
[3] Department of Earth Sciences, Utrecht University, Utrecht, The Netherlands.
[4]Department of Earth and Environmental Sciences, University of Texas at Arlington, Arlington TX, United States.
[5]Department of Civil Engineering, University of Texas at Arlington, Arlington TX, United States.
[6]Division of Data Science, College of Science, University of Texas at Arlington, Arlington TX, United States.
[7]Department of Irrigation and Reclamation Engineering, College of Agriculture and Natural Resources, University of Tehran, Karaj, Iran.
* Corresponding author. E-mail: ebrahimian@ut.ac.ir

Introduction

- Accurate soil moisture monitoring is essential for improving agricultural practices, managing drought and protecting water resources.
- HYDRUS-1D is primarily used to model solute transport in porous media using the advection–dispersion equation (ADE)
- While HYDRUS-1D is widely used for subsurface water flow and solute transport, its application to surface flow in furrow irrigation remains unexplored.

Objective

- This study introduces a novel approach using HYDRUS-1D to simulate overland solute transport during furrow fertigation by focusing solely on surface dynamics and adapting model parameters accordingly.

Methods

- The data used in this study are from a furrow fertigation experiment at the University of Tehran, Karaj, Iran (Ebrahimian et al. 2013).
- They studied nitrate transport under three open-end furrow methods: conventional (CFI), variable alternate (AFI), and fixed alternate (FFI) furrow irrigation.
- The furrows were modeled as an open-surface conduit in HYDRUS-1D, with θ_r = 0.0, θ_s = 1.0, and α = 0.0001 m^{-1}. Default values were used for n (1.56) and l (0.5), and bulk density was set to 1000 kg m^{-3}, the density of water
- Initial solute concentration was zero, with constant pressure heads (0.0) at both boundaries. A time-variable solute flux was applied at the inlet, with a zero-gradient at the outlet.
- The flow velocity (v), equal to the saturated hydraulic conductivity (K_S) optimized by HYDRUS-1D, and the dispersion coefficient (D), calculated as the product of the optimized longitudinal dispersivity (α_L) and flow velocity, were used to fit the ADE as below.

$$\frac{\partial(\theta C)}{\partial t} = -\frac{\partial(v\theta C)}{\partial x} + \frac{\partial}{\partial x}\left(D\frac{\partial C}{\partial x}\right) + S$$

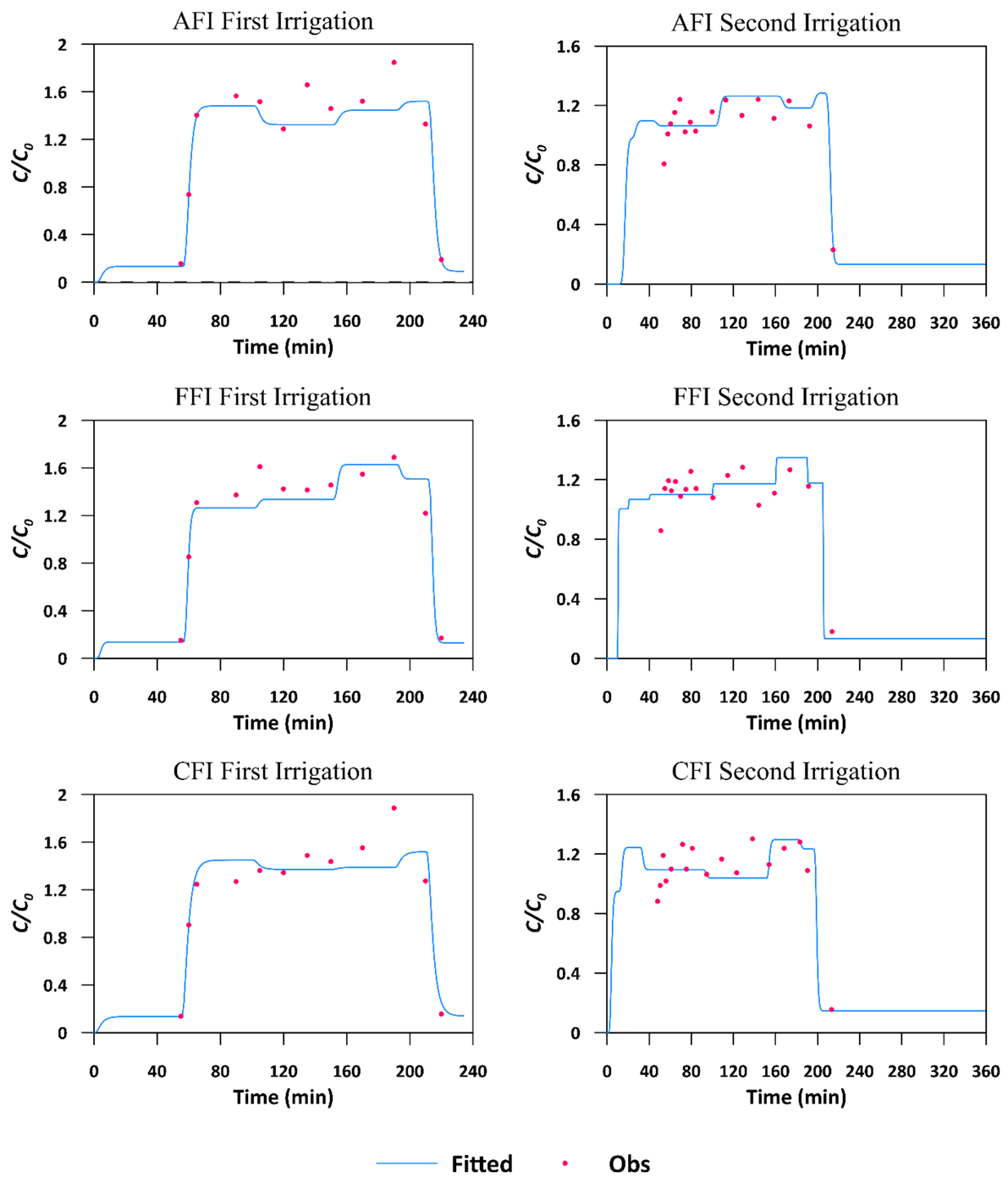

Figure 1. Measured and fitted breakthrough curves using HYDRUS-1D, showing nitrate concentrations at the furrow ends (86 m from the inlet) over time for the various treatments in the Ebrahimian et al. (2013) dataset.

Table 1. Statistical parameters obtained by fitting HYDRUS-1D to the measured breakthrough curves. HYDRUS-1D generated values for the saturated hydraulic conductivity, which in this study corresponds to the flow velocity within the furrows, as well as the longitudinal dispersivity.

Optimized parameters	Treatments					
	AFI First Irrigation	AFI Second Irrigation	FFI First Irrigation	FFI Second Irrigation	CFI First Irrigation	CFI Second Irrigation
Flow velocity (m/min)	16.2	5.0	19.4	7.9	20.2	20.4
Dispersion coefficient (m^2/min)	133.2	2.5	78.3	2.4	381.7	72.4

Table 2. Statistical parameters obtained by fitting HYDRUS-1D to the measured breakthrough curves of Ebrahimian et al. (2013) dataset.

Optimized parameters	Treatments					
	AFI First Irrigation	AFI Second Irrigation	FFI First Irrigation	FFI Second Irrigation	CFI First Irrigation	CFI Second Irrigation
R^2	0.92	0.82	0.93	0.86	0.87	0.80
RMSE (mg/L)	47.1	23.0	37.7	20.3	50.1	25.2
NSE	0.90	0.80	0.93	0.85	0.87	0.79

Results and Discussion

- Flow velocity varied by irrigation method and sequence, affecting solute residence time and spreading. The highest velocities were observed in the first and second CFI irrigations while AFI and FFI showed lower velocities, especially in the second irrigation (e.g., 5.0 m/min for AFI). The drop in velocity between cycles highlights the need for dynamic modeling across multiple fertigation events.
- Dispersion coefficients also varied, with the highest in CFI's first irrigation. The lowest occurred in FFI's second irrigation. These trends align with studies showing that alternate furrow methods can reduce leaching but may cause uneven nutrient distributions.
- R^2 and NSE ranged from 0.80 to 0.93, with the best fits in FFI's first irrigation. The lowest RMSE values occurred during slower flows in FFI and AFI, while higher RMSEs in CFI (up to 50.1 mg/L) may reflect turbulence not captured by the model.
- Unlike prior studies that used coupled surface–subsurface models (e.g., Brunetti et al., 2018), our approach focused solely on surface flow, thus simplifying simulations.
- Compared to Ebrahimian et al. (2013), who reported R^2 = 0.75, our model achieved better regression (R^2 = 0.91) and more realistic breakthrough curve predictions.

Future Work

- Future research will evaluate this modeling approach in two- and three-dimensional surface domains to assess its scalability and accuracy under more complex geometries.
- Depending on the outcomes, this functionality could be integrated into future releases of the HYDRUS software for broader use in surface irrigation modeling.
- Further studies may also explore coupling this method with real-time field data to support dynamic fertigation scheduling and improved water-nutrient management.

Acknowledgements

We used ChatGPT-3.5 for language editing. BG thanks the University of Texas at Arlington for support via startup and STARs funding.